REPUBLIC OF TURKEY

YILDIZ TECHNICAL UNIVERSITY

GRADUATE SCHOOL OF SCIENCE AND ENGINEERING

SUSTAINABLE WASTE UTILIZATION IN GLASS-CERAMIC COATING PRODUCTION

İremnur CEYLAN

MASTER OF SCIENCE THESIS

Department of Metallurgical and Materials Engineering

Material Program

Supervisor

Assoc. Prof. Dr. Buğra ÇİÇEK

July, 2022

REPUBLIC OF TURKEY

YILDIZ TECHNICAL UNIVERSITY

GRADUATE SCHOOL OF SCIENCE AND ENGINEERING

SUSTAINABLE WASTE UTILIZATION IN GLASS-CERAMIC COATING PRODUCTION

A thesis submitted by İremnur CEYLAN in partial fulfilment of the requirements for the degree of MASTER OF SCIENCE is approved by the committee on 26.07.2022 in Department of Metallurgical and Materials Engineering, Material Program.

Assoc. Prof. Dr. Buğra ÇİÇEK
Yıldız Technical University
Supervisor

Approved By the Examining Committee

Assoc. Prof. Dr. Buğra ÇİÇEK, Supervisor
Yıldız Technical University _____

Assoc. Prof. Dr. Metin GENÇTEN, Member
Yıldız Technical University _____

Assoc. Prof. Dr. Ergün KELEŞOĞLU, Member
Türk-Alman University _____

I hereby declare that throughout my thesis project entitled "Sustainable Waste Utilization in Glass-Ceramic Coating Production", I have procured all relevant legal permissions, that I have appropriately cited references and made correctly in-text citations, that I have not misrepresented research data or study results, and that I have firmly attached to the principles of scientific research and academic ethics. I must embrace any potential consequences unless a deceptive statement is revealed.

İremnur CEYLAN

Dedicated to my family

and my loved one

ACKNOWLEDGEMENTS

First and foremost, I am grateful for Assoc. Prof. Buğra ÇİÇEK’s enthusiasm and encouragement for the research. I would like to express my gratitude for his long-term support and understanding.

A particular thanks to Dr. Oğuz KARAAHMET, YTU's Metallurgical and Materials Engineer, for his invaluable assistance and guidance on all of my projects.

Thank you also to the members of the Akcoat Advanced Chemical Coating Materials Co.'s Enamel Solutions Research & Developments Departments for providing me with unique knowledge and experiences.

Beyond everything, I am grateful for my family and my love Kağan YÜCETÜRK, whose unconditional love and encouragement keep me inspired, confident, and focused. You consistently remind me of the important priorities and are always supportive of my efforts.

İremnur CEYLAN

TABLE OF CONTENTS

LIST OF SYMBOLS

°C	Celsius Degree
cm	Centimetre
cc	Cubic Centimetre
°	Degree
GPa	Gigapascal
g	Gram
h	Hour
K	Kelvin
kg	Kilogram
kJ	Kilojoule
kV	Kilovoltage
Δl	Length Change
α	Linear Coefficient of Thermal Expansion
MPa	Megapascal
μm	Micrometre
mA	Milliampere
mg	Milligram
mL	Millilitre
mm	Millimetre
min	Minute
Pa s	Pascal-second
%	Percentage
rpm	Round Per Minute
Δt	Temperature Change
β	Volumetric Thermal Expansion
wt. %	Weight Percentage

LIST OF ABBREVIATIONS

AODS	Argon Oxygen Decarburization Slag
BSE	Back Scattered Electron Mode
BOF	Basic Oxygen Furnace
BOFS	Basic Oxygen Furnace Slag
BF	Blast Furnace
BFS	Blast Furnace Slag
COE	Coefficient of Thermal Expansion
DSC	Differential Scanning Calorimetry
DTA	Differential Thermal Analysis
EAF	Electric Arc Furnace
EAFOS	Electric Arc Furnace Oxidizing Slag
EBSD	Electron Backscatter Diffraction
EDS	Energy Dispersive X-ray Spectrometer
FE-SEM	Field Emission Scanning Electron Microscopy
F	Frit
GC	Glass-Ceramic
GBFS	Granulated Blast Furnace Slag
HSM	Hot Stage Microscopy
ICP-MS	Inductively Coupled Plasma – Mass Spectrometry
IEI	International Enamellers Institute
ISO	International Standards Organization
LFS	Ladle Furnace Slag
PS	Phosphorus Slag
PEI	Porcelain Enamel Institute
SEM	Scanning Electron Microscopy
TGA	Thermogravimetric Analysis
TG-DTA	Thermogravimetric-Differential Thermal Analysis
UV	Ultraviolet
VEA	Vitreous Enamel Association
XRD	X-Ray Diffraction
XRF	X-Ray Fluorescence

LIST OF FIGURES

LIST OF TABLES

ABSTRACT

Sustainable Waste Utilization in Glass-Ceramic Coating Production

İremnur CEYLAN

Department of Metallurgical & Material Engineering

Master of Science Thesis

Supervisor: Assoc. Prof. Buğra ÇİÇEK

In the present study, the utilization of Blast Furnace Slag (BFS) waste as a sustainable, cost-effective CaO, SiO_2, Al_2O_3, and MgO replacement for inorganic oxides in the manufacturing of frit, a raw material for glass-ceramic production, was investigated. To compare a commercially available frit (F-STD) against frit made from BFS waste (F-BFS), two distinct frits were manufactured by melting-quenching techniques and characterized. The chemical composition, phase formation, and thermal characteristics of the frits, which have glassy structure, were evaluated employing XRF, XRD, heating microscopy, dilatometry, and TG- DTA analysis methods. The frits were ground and electrostatically sprayed onto a steel substrate, then crystallized at 830 °C for 4.5 minutes to obtain glass-ceramic coatings. By employing XRD, SEM-EDS, and ICP-MS; the reference (GC-STD) and BFS-substituted sustainable (GC-BFS) coatings were investigated in terms of phase formation, microstructure and chemical resistance. Ni-substituted fluorine mica ($KLiNi_2Si_4O_{10}F_2$) was the primary crystal in both samples. The higher amorphous degree of GC-BFS (70%) rather than the GC-STD (69.1%) examined at the XRD pattern of glass-ceramics was associated with the thermal characteristics of GC-BFS. Similarly, after a boiling citric acid test (ISO 28706-1: 2008), ICP-MS analysis demonstrated that the GC-BFS had an improved chemical resistance, which was consistent with the higher amorphousness with the strong amorphous structure and thermal characteristics shown in XRD and TG-DTA results.

Keywords: Sustainable manufacturing, Waste disposal, Blast furnace slag, Frit, Glass-ceramic coating

ÖZET

Cam Seramik Kaplama Üretiminde Sürdürülebilir Atık Kullanımı

İremnur CEYLAN

Metalürji ve Malzeme Mühendisliği Anabilim Dalı

Yüksek Lisans Tezi

Danışman: Doç. Dr. Buğra ÇİÇEK

Bu çalışmada, yüksek fırın cürufu (BFS) atığının, cam-seramik üretimi için hammadde olan frit üretiminde sürdürülebilir, uygun maliyetli CaO, SiO_2, Al_2O_3 ve MgO vb. inorganik oksitlerin ikamesi olarak kullanımı araştırılmıştır. Ticari olarak temin edilebilen bir friti (F-STD) BFS atığından (F-BFS) yapılan fritle karşılaştırmak için, ergitme-su verme teknikleri ile iki farklı frit üretildi ve karakterize edildi. Camsı yapıya sahip fritlerin kimyasal bileşimi, faz oluşumu ve termal özellikleri XRF, XRD, ısı mikroskobu, dilatometre ve TG-DTA analiz yöntemleri kullanılarak değerlendirilmiştir. Fritler öğütülmüş ve bir çelik alt-tabaka üzerine elektrostatik sprey yöntemi kullanılarak püskürtülmüş, daha sonra cam-seramik kaplamalar elde etmek amacıyla 830 °C'de 4.5 dakika boyunca kristalize edilmiştir. XRD, SEM-EDS ve ICP-MS analizleri kullanarak; referans (GC-STD) ve BFS ikameli sürdürülebilir (GC-BFS) kaplamalar faz oluşumu, mikro yapı ve kimyasal direnç açısından araştırıldı. Ni-ikameli flor mika ($KLiNi_2Si_4O_{10}F_2$) her iki numunede de birincil kristaldi. Cam-seramiklerin XRD modelinde incelenen GC-STD'den (%69.1) ziyade GC-BFS'nin daha yüksek amorf derecesi (%70), GC-BFS'nin termal özellikleri ile ilişkilendirilmiştir. Benzer şekilde, kaynayan bir sitrik asit testinden (ISO 28706-1: 2008) sonra, ICP-MS analizi, XRD ve TG-DTA da gösterilen daha yüksek amorfluk ve termal özellikler ile tutarlı olan gelişmiş bir kimyasal dirence sahip olduğunu göstermiştir.

Anahtar Kelimeler: Sürdürülebilir üretim, Atık bertarafı, Yüksek fırın cürufu, Frit, Cam seramik kaplama

1
INTRODUCTION

1.1 Literature Review

With the increasing human population, urbanization and industrialization, the number of waste increases daily, and it is a challenging task to maintain the supply-demand balance in raw material resources [1-2]. Thus; waste management has become a global issue due to the protection of human health, reducing environmental risks and need for less consumption of resources [3]. All products that are still industrially valuable, obtained during or after industrial activities such as production, machining, mining, refining, synthesis, heat treating, and control processes, are considered as industrial waste (IW) [4]. In order to ensure sustainability by recycling or reusing IWs such as sand, ash, slag, to reduce the burden on the industry and to diminish the potential threats, variety of methods have been developed [5]. Incineration, recovering through calcination, vitrification are some of the sustainable approaches rather than accumulating in landfill [6]. Among them the vitrification method is the stabilization of diverse inorganic wastes and metal elements by chemically bonding them to amorphous networks in a glassy structure by thermal fusion process [7]. Vitrification processes include the melting of waste combined with glass forming and network modifiers etc. at high temperature and then quenching to achieve an amorphous structure [8]. The vitrification of IWs combined with commercial sources and glass-ceramic production by crystallization are detected in the literature with the following examples: fly ashes [9-10], muds [11], slags from crude iron and steel production [12-13], cullets [14-15], furnace dust and foundry sands [16-17].

One of the most common IWs is blast furnace slag (BFS), which is a by-product that accumulates on the upper surface of molten iron during iron production from ore in a blast furnace [18]. It has an alumina silicate structure containing oxides of calcium (Ca) and magnesium (Mg) [19]. The chemical composition of BFS is mainly 35-42 wt.% CaO, 35-40 wt.% SiO_2, 8-15 wt.% Al_2O_3, and 5-9 wt.% MgO, with minor components of 0-5 wt.% BaO, 0.3-3 wt.% MnO, 0.5-0.8 wt.% FeO, and 0.7-1.5 wt.% S [20]. The world output of BFS in 2019 is estimated to be between 320-384 million tons, according

to the US Geological Survey Mineral Commodity Summaries [21-22]. To ensure the recycling of high tonnage BFS waste, it is significant to employ BFS in areas with different and wide raw material consumption volumes. Although there are studies in the literature regarding BFS utilization in ceramics, glass-ceramics and cement products, it will be shown for the first time in this publication that BFS can also be successfully adapted to glass-ceramic coatings on metal substrates which are commercially named vitreous enamels.

Zhao et al. [23] manufactured glass-ceramic system of $CaO–Al_2O_3–SiO_2–MgO$ by directly heating them with molten glass including BFS and silica sand rather than room temperature glass. The behaviour of the glass during crystallization and the influence of CaF_2 on its microstructure are also examined. The $SiO_2–CaF_2–BFS$ mixture was melted at 1500–1600 °C, cast into a mould, and annealed at 960 °C for 1.5 h to produce $CaO–Al_2O_3–SiO_2–MgO$ glass ceramics with akermanite ($Ca_2MgSi_2O_7$) and diopside ($CaMgSi_2O_6$) phases in the research.

In the study [24] by Y. C. Wang et. al, blast furnace slag (BFS) glass ceramics containing Cr_2O_3 were added to overcome scum in the liquid glass and enhance phase separation and crystallization was investigated. The chemical composition of glass-ceramics is 31 wt.% CaO, 49 wt.% SiO_2, 11 wt.% Al_2O_3, and 9 wt.% MgO, were prepared with 73 wt.% BFS and the other raw materials of quartz sand and a small amount of pure chemical reagents. The glass-ceramics were characterized by Differential Thermal Analysis (DTA), X-ray Diffraction (XRD), Scanning Electron Microscopy (SEM), and flexural strength. It is possible to create a process for producing high-value glass ceramics using molten BFS as the primary raw material. This is critical for increasing the usage and added value of iron smelting slag while also decreasing environmental pollution. Uniform diopside crystals can be obtained, these glass-ceramics are much higher than mechanical properties of natural granite and natural marble, when the Cr_2O_3 is 1.44 or 1.91 wt.%.

Francis [25] investigated the devitrification characteristics of different diameters of slag-derived glass and researched the implementation of BFS into glass-ceramic materials. With no additive components, the BFS was melted, then cast into a heated mould, annealed, powdered, and sorted into particle size ranging. DTA, XRD, and SEM analysis were employed to examine samples that crystallized into gehlenite

($Ca_2Al_2SiO_7$), diopside pyroxene ($Ca(Mg,Al)(Si,Al)_2O_6$), and barium aluminium silicate ($BaAl_2Si_2O_8$) phases.

By melting Na_2CO_3 and Cr_2O_3-added BFS at 1450 °C, casting, and annealing at high temperatures (800–900 °C), Ma et al. [26] produced $CaO–MgO–Al_2O_3–SiO_2$ glass-ceramics. To describe the glass-ceramics in terms of crystallization properties, kinetic parameters of crystallization, microstructure, and orientation relations, they used differential scanning calorimetry (DSC), XRD, SEM, and Electron backscatter diffraction (EBSD) study.

Glass-ceramic coatings industrially known as enamel coatings are produced by vitrification and crystallization of inorganic oxides such as SiO_2, B_2O_3, CaO, Na_2O, P_2O_5, CuO, Al_2O_3 etc. and are crystalline materials embedded in a glass matrix. Their production requires five main steps: i) formulation and preparation of raw material batch, ii) the vitrification procedure consisting of the melting of inorganic oxides at 1300 °C ± 100 °C and subsequent fast-cooling i.e., quenching to obtain glassy structure, iii) milling and sieving of the glass precursor, i.e. frit, to obtain powder, iv) application of the powdered frits on the metal substrate, v) sinter-crystallization at 720-850 °C [27-29]. Glass-ceramic coatings protect the surfaces of kitchen utensils, pipelines, home appliances, boilers, as well as other objects against chemical, mechanical, and thermal deterioration [29]. Glass-former, modifier, stabilizer, and promoter oxides are the primary parameters that define the glass-ceramic structure and provide it high technical characteristics [30].

By integrating BFS waste as a source of CaO, SiO_2, Al_2O_3, and MgO with commercial raw materials, the current research intends to provide a new strategy for the achievement of sustainable glass-ceramic coating. Two distinct frit batches (F) were created and analysed to examine whether BFS waste could be successfully incorporated into glass-ceramic coatings. Frits composed entirely of commercially available raw materials and formulations containing partial amounts of BFS were designated F-STD and F-BFS, respectively. The chemical composition, phase transition, and thermal behaviour of the frits were analysed using XRF, XRD, heating microscopy and TG-DTA. SiO_2-B_2O_3-Na_2O-Al_2O_3-K_2O-F glass-ceramic coatings were formed after the frits were coated to metal substrates by electrostatic spraying method, crystallized at 840 °C for 4 min., and referred to as GC-STD and GC-BFS, respectively. XRD and SEM-EDS were used to characterize GC-STD and GC-BFS in terms of micro and macrostructure,

phase formation, and surface morphology. Furthermore, the engineering properties of coatings as adhesion behaviour, chemical resistance and aesthetical properties of coatings were investigated according to BSI EN10209, ISO 28706-2 and ISO 7724, respectively.

1.2 Objective of the Thesis

The earth's crust provides the raw materials require to produce glass-ceramics. However, demand will soon overbalance the supply with increasing population and industrialization. This problem was addressed, and the raw material resources utilized in glass-ceramic raw material (frit) production have been replaced by the blast furnace slag (BFS) from the sustainability perspective. The aim of this study is to achieve not only glass-ceramic but also a novel and eco-friendly production approach of glass-ceramic coating on a metal substrate by recycling the BFS one of the most common IWs. In this research, a SiO_2-B_2O_3-Na_2O-Al_2O_3-K_2O-F glass ceramics system was studied to offer a coating material that had never been elucidated in the literature before.

1.3 Hypothesis

Our study provides a significant contribution to the literature as it serves as the basis for the sustainable production and comparative investigation of coatings based on SiO_2-B_2O_3-Na_2O-Al_2O_3-K_2O-F glass-ceramic systems using partially BFS. It is formed during the iron production process in blast furnace and consists of CaO, SiO_2, Al_2O_3, MgO as major components and MnO, FeO, BaO and S etc. as minor components. Our hypothesis is that as-received BFS can be utilized as sustainable CaO, SiO_2, Al_2O_3, MgO etc. raw material sources in the raw material batch of production of glass-ceramic coating on a steel substrate, due to the chemical composition of BFS. Frit, glass-ceramic and glass-ceramic coatings that will be produced by commercial and sustainable methods will be analysed and it will be examined whether BFS can be an appropriate raw material for use in the structure and whether it will alter the engineering properties of the coating.

2
GLASS-CERAMICS

Glass-ceramics are polycrystalline materials produced by heat treatment from inorganic glasses. Controlled nucleation and crystallisation of glass are achieved through heat treatments in glass-ceramic production [31-32]. Glass-ceramics are ideal for coating applications due to their chemical stability, high mechanical strength, low thermal expansion coefficient, thermal shock resistance, and abrasion and corrosion resistance.

2.1 Definition of Glass-Ceramics

Dr. S.D. Stookey, a well-known glass chemist, discovered and defined glass-ceramics in the 1950s. "Glass-ceramics are made by first melting and forming special glasses containing nucleating agents, then causing controlled crystallisation of the glass," according to Dr. Stookey [33].

The fact that this definition was created on this date does not preclude the existence of such materials in previous years. In the 1700s and even earlier, scientists used glass crystallisation to create dense ceramic materials. Dr. Stookey became aware of this material, investigated it deeply, and then commercialised it as a new type of material. In that laboratory, he was conducting a silver precipitation experiment with lithium silicate glass for permanent photographic image work. The use of lithium silicate is due to the fact that lithium glasses are more chemically stable. For precipitation research, Stookey holds the glasses at nearly 450 °C, and the furnace temperature increases to 850 °C one night. Stookey, who had assumed the glass had melted and the furnace had been ruined, discovered that the sample had not melted and remained in the same condition as when it had left. The glass fell to the ground accidentally while being removed from the furnace, but it did not shatter. It sounds like metal, on the contrary. Stookey inspects the glass after this bizarre situation. Knowing the importance of crystals with low expansion coefficient over the studies on the near-zero thermal expansion of β-spodumene in previous years [34].

Stookey is still researching this topic and working with crystals such as titania, zinc sulphide, and others. He sees the strength of Titania-doped aluminosilicate glass-

ceramics in his work with Titania and commercialises it through Corning Ware®, a product that is even used in rocket nose cones.

Over time, these glass-ceramics have evolved, and their applications have expanded. Due to advancements in other ceramic, glass, metal, and nanomaterial fields, all fields have become associated, and glass-ceramic materials have become mixed with glass-crystal composites. Deubener et al. give the following definition of glass-ceramics: "Glass-ceramics are inorganic, non-metallic materials prepared by controlled crystallisation of glasses via various processing methods." They have a residual glass and at least one type of functional crystalline phase. "The volume fraction crystallised can range from ppm to nearly 100%." Inorganic materials produced by controlled nucleation and crystallisation of glasses are known as glass-ceramics [35-36].

They are polycrystalline materials that use controlled heat treatment to replace nucleation and crystal growth processes in glasses appropriate for crystallisation. During the crystallisation process, nucleating agents are mixed into the glass matrix. Nucleating agents are mainly TiO_2 (titanium dioxide), Cr_2O_3 (chromium (III) oxide), ZrO_2 (zirconium dioxide) and P_2O_5 (phosphorus pentoxide) oxide groups and fluorides. Within the matrix, these oxides act as nucleation centres. As a result, these nuclei grow and form crystals during the controlled heat treatment step. During crystallisation, one or more crystalline phases form, and these crystals can take a variety of shapes, including rods, sheets, and spheres. The crystals formed are usually less than 1 m in size, and they give glass-ceramic structures properties like superior toughness, impact resistance, and wear resistance [35-37]. Formation of glass-ceramics is shown in Figure 2.1.

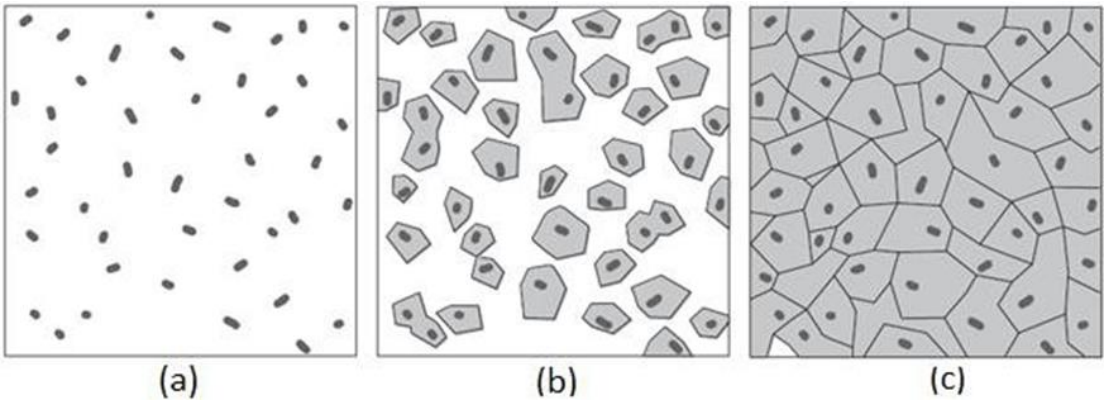

Figure 2.1 From glass to glass-ceramic. (a) nuclei formation, (b) crystal growth on nuclei, and (c) glass-ceramic microstructure [35]

The goal of crystallisation heat treatment, also known as controlled crystallisation, which is the main stage of glass-ceramic production, is to convert amorphous glass into microcrystalline ceramic. The effect of temperature on nuclei formation and crystal growth is shown in Figure 2.2. The tendency of any glass to nucleate and grow crystals can explain its crystallisation. Below the equilibrium melting temperature, if a sufficient number of nuclei (at least 10^{12} – 10^{15} nuclei in 1 cm^3 volume) is achieved by heterogeneous nucleation, a semi-stable region temperature range occurs where crystal growth can occur [38-39].

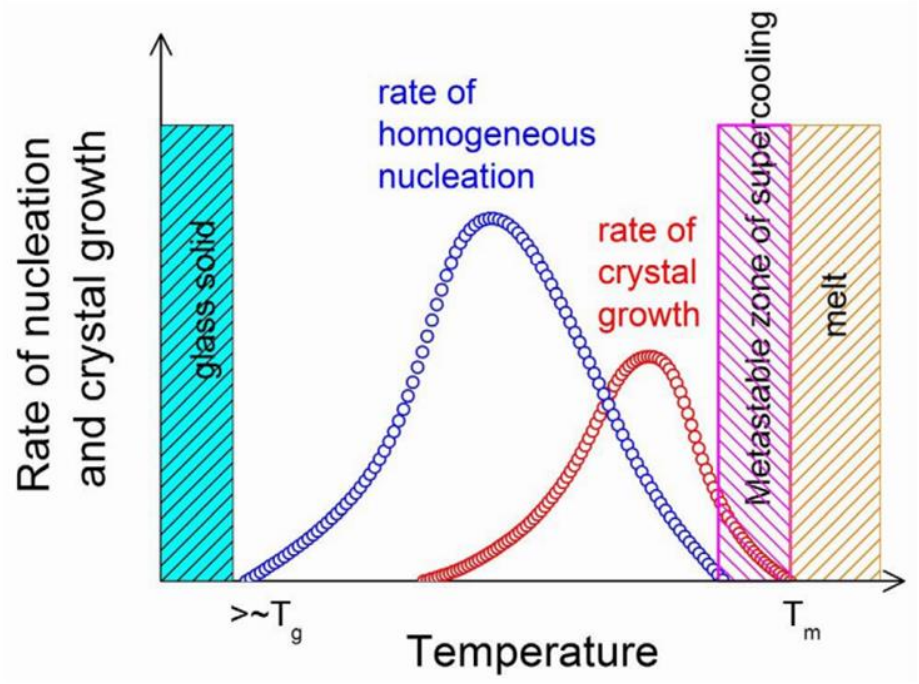

Figure 2.2 The effect of temperature on nucleation and crystal growth in glasses [40]

2.2 Formation Methods of Glass-Ceramics

2.2.1 Pressing

The glassware is shaped by applying pressure between a mould and a plunger in this method. Air vacuum, metal presses, and other types of pressing equipment can be used.

2.2.2 Casting

The glass viscosity must be minimal and the temperature must be over the glass transition temperature for using this ancient technique. This technique could be applied in the dental area.

2.2.3 Spinning (Centrifugal Casting)

The necessity for a conical mould which should rotate separates this method from standard casting. In this process, the viscosity must be between 30 and 100 Pa s [35]. This is how old-fashioned cathode ray tubes of television bulbs were made.

2.2.4 Rolling

The rolling method involves pouring molten glass onto a water-cooled press table and rolling it out. The ideal viscosity is 700–1000 Pa s. This method can be used to create flat glasses [35].

2.2.5 Float Process

The basic forming in a molten tin bath is the float or Pilkington process, which is nowadays most commonly used in flat glass production. The molten glass is flattened and strengthened in the tin bath at low temperatures since it arrives from the furnace belly. The flat glass continues on the same conveyor line, enters the annealing line, lowers the tension, and continues.

2.2.6 Direct Forming or Reforming of Glass-Ceramics

Glass-ceramics can be made from ceramic phases in some circumstances. The remaining glass phases soften, making it possible to shape them.

2.3 Properties of Glass-Ceramics

Because of their thermal properties, glass-ceramic materials do not shrink during production. As a result, they can be found in a wide range of industrial and technological uses, particularly in kitchenware. Crystals and microstructure control can be used to reach desired transparency and opacity values due to their glassy phase and nonporous structure. Another optical feature of glass-ceramic applications is that they can achieve any desired colour. When chemicals interact with glass-ceramics, they have advanced chemical properties due to the crystal structure, glass structure, and chemical durability property. Mechanically, flexural strengths of up to 500 MPa have been achieved, and toughness values of more than 3 $MPa.m^{1/2}$ have been achieved with the developments [18, 35, 41, 42].

2.4 Application Areas of Glass-Ceramics

Because of their superior engineering properties, glass ceramics can be used in a wide range of industrial applications. Some of these application areas are given in Table 2.1.

Table 2.1 The main crystalline phases, properties, and application areas of some glass-ceramic systems [37]

System	Main Crystalline Phase	Property	Application Area
$Li_2O.Al_2O_3.SiO_2$ (ZrO_2, TiO_2)	β-quartz β-spodumene β- eucryptite	Low thermal expansion High temperature resistance	Kitchenware Telescope Mirrors Oven Tops
$Li_2O.Al_2O_3.SiO_2$ (P_2O_5)	$Li_2O.Al_2O_3.SiO_2$	Dielectric properties Chemical resistance	Electronic Insulation Optical Coding Magnetic Recording Head Electric Sleeve
MgO. $Al_2O_3.SiO_2$ (P_2O_5, TiO_2)	Cordierite ($Mg_2Al_4Si_5O_{18}$)	Radar permeable Low thermal expansion High strength	Missile Cap Radar Dome
$PbO.ZnO.B_2O_3.SiO_2$ (F)	Rankinite ($3CaO.SiO_2$)	Heat & Vacuum insulation	Electrotechnology Microelectronic Circuits Capacitor
$BaO.Al_2O_3.SiO_2$ (TiO_2)	Celsian ($BaAl_2Si_2O_8$) Barium Titanate ($BaTiO_3$)	High strength Thermal shock resistance	Kitchenware Cookware
$SiO_2.Al_2O_3.MgO.K_2O$	Phlogopite[$KMg_3AlSi_3O_{10}(F,OH)_2$]	Turning ability Dielectric properties	Electrotechnology Insulator Hermetic Seals
$SiO_2.CaO.Na_2O$ (P_2O_5)	Apatite $Ca_5(PO_4)_3(F,Cl,OH)$	Biocompatibility Chemical resistance	Dentistry Prothesis
$SiO_2.Al_2O_3.MgO$ (TiO_2)	Mg-Al Titanate $Mg_xAl_{2(1-x)}Ti_{(1+x)}O$	High hardness Resistance	Construction
$SiO_2.Al_2O_3.CaO$ (ZnO)	Wollastonite ($CaSiO_3$)	High hardness Resistance	Architectural Materials
$SiO_2.Al_2O_3.MgO.CaO$ (Sulphide, fluoride)	Wollastonite ($CaSiO_3$) Anorthite ($CaAl_2Si_2O_8$) Diopside ($MgCaSi_2O_6$) Pyroxene [$(Na,Ca)_n(Mg,Fe,Al)(Al,Si)_2O_6$]	High hardness Abrasion resistance Chemical resistance	Floor Tile Exterior Architectural Materials Pump Pipe

2.4.1 Technical Applications

Radomes were the first glass-ceramics to be commercially available. The radar antenna is protected by a structural, weatherproof enclosure. The electromagnetic signal transmitted or received by the antenna is diminished to a minimum by Radom glass-ceramic, which is sensitive to radio waves. This type of application necessitates a low dielectric loss, low dielectric constant, low coefficient of thermal expansion, high strength, and high abrasion resistance [43].

Electronics, chemistry, acoustics, optics, mechanics, and biology all benefit from photosensitive and etched patterned materials, which are manufactured in extremely sensitive miniature sizes for use in electronics, chemistry, acoustics, optics, mechanics, and biology. The SiO_2–Li_2O system is commonly used to create these types of glass ceramics. Ce^{3+} and Ag^{+} ions make up the parent glass. Photoelectrons cause the oxidation of Ce^{3+} to Ce^{4+} and Ag^{+} to Ag^{0} in the compositions when exposed to UV. Crystal phases are precipitated through controlled crystallisation during the heat treatment at 600 °C [44].

Lithium metasilicate crystals are etched with dilute hydrofluoric acid to produce the final product. Corning Glass marketed these refined glassy bodies under the Fotoform® trademark. With a few modifications, the non-etched structure was marketed as Fotoceram®.

Glass-ceramics with fluoromica are machinable GCs. The fluorphlogopite phase is present in the most well-known machinable commercial glass-ceramic, MACOR® ($KMg_3AlSi_3O_{10}F_2$). Macor is utilised in a variety of applications, including spacecraft boundary retainers, electrical insulators, suction feedthroughs, microwave-type component screens, field-ion microscope parts, seismograph coils, and gamma-ray lens frames [45].

GCs can also be found in magnetic memory discs. The most common GC used for this purpose are canasite, lithium disilicate, spinel–enstatite, and spinel. For this type of material, nanostructured fracture toughness and young modules are crucial. For example, the solid solution of Gahnite type, $ZnAl_2O_4$, or spinel type, $MgAl_2O_4$, or the solid solution of both types of crystals must be smaller than 0.1μm, enstatite fracture toughness is greater than 1MPa $m^{1/2}$, and spinel–enstatite material has a Young's

modulus of 100–165 GPa, which is actually high in comparison to other GC materials, which is the best-known option for magnetic memories [35].

Substrates for Liquid Crystal Displays (LCD) in personal laptop computers are made using the SiO_2–Al_2O_3–Li_2O system. The GCs become transparent when the wavelength of visible light is larger than the crystallite size, and the crystals have nearly the same refractive index as the parent glass.

2.4.2 Optical Applications

Due to various temperature fluctuations, Telescope Mirror Materials required a near-zero coefficient of thermal expansion. This requirement is fulfilled by β-Quartz Solid-Solution GCs. The Integrated Lens Array was made from lithium metasilicate/lithium disilicate glass-ceramics with a thickness of about 20 m [46].

Because of their energy efficiency and reduced data loss, Luminescent Glass-Ceramics are becoming increasingly popular. Cr-Doped Mullite for Solar Concentrators, Cr-Doped Gahnite Spinel for Tunable Lasers and Optical Memory Media, Rare-Earth (such as Ytterbium, Erbium, Praseodim, etc) Doped Oxyfluorides for Amplification, Upconversion, and Quantum Cutting, Chromium (Cr^{4+})-Doped Forsterite, β-Willemite, and Other Orthosilicates for Broad Wavelength Amplification, Ni^{2+}-Doped Gallate Spinel for Amplification and Broadband Infrared Sources, Yttrium-(gadolinium)-aluminate garnet glass-ceramic Phosphor for White LED were good examples for luminescent GCs [35].

Optical Components such as Fiber Bragg Grating Athermalization, Laser- Induced Crystallization for Optical Gratings and Waveguides, Ferrule for Optical Connectors, Transparent ZnO Glass-Ceramics with Controlled Infrared Absorbance and Microwave Susceptibility were also made of different crystal- based GCs [47].

2.4.3 Medical and Dental Glass-Ceramics

This title encompasses two distinct applications: implantology (medical prostheses) and materials used in restorative dentistry (dental prostheses) [48].

Medical prostheses for orthopaedics, head and neck surgery, dental implants, and root fillers are all made with implantology. All of them have one thing in common: they're inserted into the human body. Restorative dentistry materials are not inserted into the body. They're instead used to restore natural teeth. This category includes dental inlays,

crowns, bridges, and veneers, to name a few. Although the materials in these two groups appear to be similar, they are completely different. Biocompatible and bioactive materials are required for implantology. Bioactive materials have a biologically active hydroxycarbonate apatite layer that allows them to bond with bones and even soft organs. Implant materials may be subjected to mechanical forces, necessitating the use of strengths such as compression, tensile, shear, toughness, and Young's modulus. Visual characteristics are frequently overlooked. Unlike implant materials, restorative dental application materials must be aesthetically pleasing and look like natural teeth. They must also be resistant to abrasion and corrosion, and they must not react with any chemicals found in foods and beverages. Both types of materials require a great deal of attention during production. Dimensional accuracy should be measured in micrometres, and the surface properties should be completely smooth or rough depending on the desired level of roughness. For these materials, different production methods such as sintering, moulding, or machining using computer-aided design (CAD)/computer-aided manufacturing (CAM) techniques can be used.

2.4.4 Electrical and Electronic Applications

Insulator materials are made with mica-type GCs. High dielectric constants are found in these materials. To create composite materials with a high dielectric constant, SiO_2-TiO_2-Nd_2O_5 and SiO_2-Al_2O_3-PbO GC systems are combined with sintered ceramics. These inorganics are combined with a binder resin (butyl methacrylate), a solvent (toluene), and a plasticizer (dibutyl phthalate) and Doctor Blade Technique applied to a smooth flat surface with a thickness of 0.1 to 0.3 mm, then temperature was increased at 400 °C to burn out the organics and sintered at 900 °C to acquire mechanically strong dense material. After the organics have been mixed, circuit patterns are siren printed on the surface [49].

GC systems are also utilised in electronic packaging. To achieve composite materials, SiO_2-Al_2O_3-MgO and SiO_2-Al_2O_3-ZnO systems are combined with advanced ceramics like ZrO_2. IBM's special computers have used this packaging system for multilayer chip carriers.

Dielectric Glass-Ceramics for GHz Electronics require special GCs. Dielectric oxide ceramics have proven to be a game-changer in the microwave wireless communication industry. They manufacture resonator and antenna components for a wide range of

applications, including cell phones and GPS systems. However, these ceramics have some disadvantages that are irrelevant to their electrical properties, the most notable of which are porosity, which causes metallization problems, and inhomogeneity, which causes performance degradation. As a result, glass-ceramics in the SiO_2–B_2O_3–TiO_2–ZrO_2–La_2O_3–RE_2O_3 system have been designed to meet the requirements of existing ceramics while also being extremely homogeneous and porosity-free. Typically, glass compositions are chosen to precipitate either $La_2Ti_2SiO_9$ or $La_4Ti_9O_{24}$, or both.

2.4.5 Architectural Applications

Nippon Electric Glass develops the most important glass-ceramic for building applications under the NeopariésTM trademark [50].

The glass-ceramic is made in the following way: To make the foundation glass, granular glass particles are used. In a totally automated process, the granular glass is shaped into flat or curved panels in a tunnel furnace at temperatures up to 1100 °C. During the heat treatment, the granular glass is sintered at 850 °C. Temperatures above 950 °C cause wollastonite to crystalize. Weathering resistance, zero water absorption, lighter weight than natural stone building materials, harder than natural stone, and so on are all important properties for these types of materials. Fire-resistant windows fall into this category as well.

2.4.6 Glass-Ceramics for Energy Applications

Several applications aimed at increasing the efficiency with which energy is produced and managed use glass-ceramics as a critical part. Glass-ceramics are used in at least three areas for energy generation: (i) solar energy efficiency, (ii) battery components, and (iii) solid oxide fuel cells [51].

Batteries have three main components: cathode, anode, and electrolyte, and GCs can effectively replace all three. The parent glass, for example, has a batch composition of Li_2O–Fe_2O_3–P_2O_5–Nb_2O_5 from which this phase is formed. Heat treatment was used to begin the crystallisation process after the glass was melted in a reducing environment. As a result of this method, $LiFePO_4$ crystallised in a continuous phase. In the glass-ceramic state, this crystal is chemically resistant to charge-discharge intercalation cycles and has a higher thermal conductivity than when formed through a solid-state reaction. As a result, when compared to a $LiFePO_4$ ceramic battery, the glass-ceramic battery has lower internal resistance and better high-rate discharge performance.

3
GLASS CERAMIC COATINGS

Glass-ceramic coatings also referred to as enamel coatings, are an excellent technology for preserving metal substrates and prolonging the life of metal products [52-53].

Mill additives along with other frit and flotation compounds, opacifiers, and colorants are comprised of the glass-ceramic coating formulation [15, 54, 55].

Frit that has amorphous structure is the main components of the glass-ceramic coating structure, it is essentially glass granules or flakes generated by melting a variety of inorganic oxides at 1000-1500 °C and rapidly cooling process. Frit is powdered in ball mills to achieve a uniform particle size [56-57].

The suspension is achieved by attaching water into the powdered frit and milling additives, it is applied to the metal substrate using the wet application methods for glass-ceramic coating include flow coating, spraying, dipping, electrophoretic deposition. On the other hand, powdered frits can be applied on metal substrates using thermal spray coating, and electrostatic powder spraying for dry application to obtain glass-ceramic coatings on metal substrate after crystallization procedure [54, 57, 58].

The devitrification stage begins after the frit powder is applied to the substrate. The characteristics of the devitrification or crystallization procedure change based on the coating formulation and the metallic substrates. Glass-ceramic coatings adhered to steel substrates are heated at temperatures ranging from 780 °C to 850 °C, whereas glass-ceramic coatings applied to aluminium substrates are heated at temperatures ranging from 500 °C to 570 °C [54, 58].

3.1 Definition of Glass-Ceramic Coating on Metal Substrates i.e. Enamel

The word enamel is derived from the elevated German word "smelzan" and the old French word "esmail." [59]. Enamel word is now referred to as "smalto" in Italian, "email" in French, and "email" in German [60].

Enamel is an inorganic glass-ceramic coating with a high heat capacity, great hardness and durability, chemical stability, and resistance to abrasion due to the silicates through

its molecular structure. ISO (International Standards Organization) defines enamel in 25.220.50 coded title as “substantially vitreous, or glassy, inorganic coating bonded to metal by fusion at a temperature above 500 °C” [61], VEA (Vitreous Enamel Association) explains enamel as “simply a thin layer of glass fused at high temperature on to the surface of a metal” [59], PEI (The Porcelain Enamel Institute, Inc.) characterize enamel as “substantially vitreous or glassy inorganic coating bonded to metal by fusion at a temperature above 426.67 °C” [62] and IEI (The International Enamellers Institute) describe enamel as “A natural material that is born from fire, is immune to corrosion and as pure as glass, comes in a huge range of colours that remain unaffected by time and atmospheric conditions, can always be recycled. A coating that offers a global, utterly versatile response to the requirements of all sorts of industrial sectors” [63].

Glass-ceramic coatings is prepared by milling the frits into powder and applying it to metallic surfaces like ferrous or non-ferrous such as aluminium and copper, finally heated at temperatures ranging from 500 to 870 °C. The melt of the inorganic oxides is quenched. This process generates the amorphous structure that allows regulated crystallization is referred to as "frit". Electrostatic spraying, wet spraying, electrophoretic deposition, dipping, and more contemporary thermal spray techniques are all used to apply glass-ceramic coating.

3.2 Chemical Structure of Glass-Ceramic Coatings

Glass-ceramic coatings are made up of structures known as "frit" that has amorphous structure. They are semicrystalline glassy coating materials obtained by vitrification and recrystallization of oxides such as SiO_2, B_2O_3, Al_2O_3, Na_2O, NiO, CuO, P_2O_5, Fe_2O_3 in accordance with the Seger formulation [15]. Its production is grouped into four categories: i) high-temperature fusing-quenching thus obtaining frit, ii) milling of frit with or without milling additives, iii) application of milled frit to the metal substrate, iii) crystallization stage at relatively high temperatures (720-850 °C) [35]. An aesthetic coating material that is resistant to mechanical, chemical, and thermal damages is obtained based on the crystal and amorphous structure generated at the conclusion of the procedure [18].

In Table 3.1, the oxides can be categorized based on their functionalities in the glass-ceramic structure. In glass-ceramic systems, silica possesses the ability to form glass at

a sufficiently high temperature (above 1700 °C) without using any other components. In glass-ceramic formulations, SiO_2 is the most utilized component than other glass-ceramic components. The vitreous coating such as glass-ceramic coatings are a silica tetrahedra network with other materials brought in as modifiers. Low melting point components consist of one or two parts of SiO_2 per part of other components and melt at temperatures of 1050 °C or lower, whereas compositions that melt at 1250 °C or higher contain three to five parts of SiO_2. The most significant disadvantage of SiO_2 as a coating ingredient is its extremely high melting point (more than 1700 °C) [16].

Table 3.1 Raw materials of glass-ceramic coatings, minerals and the functions of the components [64]

Component	Minerals	Functions
SiO_2	Quartz Feldspar	Refractory component, glass forming oxide, hardens the vitreous system, adds chemical resistance and increases viscosity.
B_2O_3	Borates	Flux that produces the vitreous matrix, reduces viscosity and increases surface hardness.
Na_2O K_2O Li_2O	Albite Feldspar Microcline Spodumene Petalite Lepidolite	Alkaline components that lower the temperature at which glass softens, reduce its elasticity and increase its brilliance.
Al_2O_3	Feldspar Corundum	Increases viscosity and chemical, mechanical and thermal resistance, reduces the expansion coefficient and favours an opaque finish.
ZrO_2	Zirconium	Improves resistance to acids, to knocks and to shocks, acts as an opacifier.
ZnO	Zincite Blende Wurtzite	Excellent flux, lowers the expansion coefficient and improves brilliance and surface quality.
CoO	Cobaltite	A very strong adherence agent, it produces a structure with lots of small, well distributed bubbles.

Table 3.1 Raw materials of glass-ceramic coatings, minerals and the functions of the components [64] (devamı)

Component	Minerals	Functions
NiO	Niccolite	A second adherence agent, it produces a structure with a small number of large bubbles.
CuO	Copper Oxide	When combined with primary bonds, it triggers the adherence reaction at lower temperatures.
MnO_2	Manganese Dioxide	Produces brown-coloured frits, intensifies dark colours and acts as an oxidant and as a weak bonding agent.
Sb_2O_3	Antimonite	Produces a high degree of opacity and improves resistance to acids.
TiO_2	Rutile Anatase	Opacifiers, it increases whiteness, brilliance and resistance to acids and heat.
BaO	Baryte Witherite Calcite	Alkaline-earthy components that integrate anti- acid glass-ceramics coating, increasing their resistance, their smelting facility and their viscosity.
CaO MgO	Dolomite Limestone Periclase	
P_2O_5	Apatite	Alters the opacity of the finish, improves colour stability and reduces chemical resistance.
F_2	Fluorite	Softens glass and influences the opacity

Table 3.2 The classification of oxides according to their functions in the glass structure

Glass Former	Glass Modifier	Glass Modifier	Adhesion Agents	Nucleating Agents
SiO_2	MgO	Li_2O	MnO_2	TiO_2
GeO_2	CaO	Na_2O	CoO	ZrO_2
B_2O_3	SrO	K_2O	NiO	Fe_2O_3
P_2O_5	BaO			Cr_2O_3
Sb_2O_5	ZnO			

The function of the components in the chemical structure of glass-ceramic coatings divide the oxides utilized into five categories: fluxes, refractories, adhesion agents, opacifiers, and colorants.

3.2.1 Fluxes

The primary purpose of this class of flux oxides is to lower the melting point of SiO_2, also the consistency of the glass-ceramic coatings are improved by the oxides in this class. The consistency appropriates improves the adherence between glass-ceramic coatings and the substrate and enhances the surface quality. Borax ($Na_2[B_4O_5(OH)_4]\cdot 8H_2O$), soda ash ($Na_2CO_3$), soda nitrate ($NaNO_3$), fluorspar ($CaF_2$), cryolite ($Na_3AlF_6$), barium carbonate ($BaCO_3$), magnesium carbonate ($MgCO_3$), litharge (lead (II) oxide), red lead (lead (II, IV) oxide), and zinc oxide (ZnO) are some of the common feedstock in this class [65].

3.2.2 Refractories

This class of material contributes to the formation of the glass mesh and aids the acidic fraction of the melt. Quartz, feldspar, and clay are the most important components in this class. As a glass-former, quartz influences the mechanical and chemical qualities of the final network [65].

3.2.3 Adhesion Agents

The adherence property of the interface which is formed in between the glass-ceramic coatings and the metallic substrate is very significant. For this reason, oxides in the

melting such as CoO (cobalt oxide), NiO (nickel oxide), and CuO (copper oxide) are employed. CoO (cobalt oxide) is the most essential adhesion agent, as it not only offers adhesion but also serves as a blue colorant [65].

3.2.4 Opacifiers

The primary duty of oxides in this class is to provide opaque glass-ceramic coatings. Opacifying oxides can be listed as Sb_2O_3 (antimony oxide), $NabO_3$ (sodium antimonate), TiO_2 (titanium dioxide), $ZrSiO_4$ (zirconium silicate), and ZrO_2 (zirconium oxide). The refractory features of these oxides are distinctive, also additional supplemental opacifiers, such as Na_3AlF_6 (cryolite) and CaF_2 (fluorspar), enhance the melt's fluidity [65].

3.2.5 Colour Agents

Glass are a kind of coating that stands out because of their exceptional technical qualities and their aesthetic qualities, as well as various colours and tints. CoO (cobalt oxide), CuO (copper oxide), FeO (iron oxide), and NiO (nickel oxide) are the most utilized oxides in this class. These colour agents can be used as colorants without the addition of any other ingredients, or pigment can be added to frits to act as a colorant [65].

3.3 Adhesion Mechanism Between Glass-Ceramic and Metallic Substrate

3.3.1 Diffusion Theory

At the interfaces between the glass-ceramic coating and the metallic substrate, iron diffusion from the metallic substrate to the glass-ceramic material and silicon diffusion from the glass-ceramic to the substrate material occur. As a result, the diffusion process is thought to contribute to the adhesion mechanism [66].

3.3.2 Chemical Theory

In this theory, when the glass dissolves the existing oxide layer and encounters the metal during sintering, a driving force occurs for the metal to oxidize and create the iron oxide (FeO) molecule [67].

Reactions occurring in the substrate material during the firing of glass-ceramic coating;

$$Fe_3O_4 \rightarrow Fe^{2+} + 2Fe^{3+} + 4O_2 \quad (3.1)$$

$$2\,Fe^{3+} + Fe \rightarrow 3Fe^{2+} \quad (3.2)$$

Fe reduces CoO (cobalt oxide) and NiO (nickel oxide) molecules in glass-ceramic coating composition to obtain metallic cobalt and nickel;

$$Fe + CoO \rightarrow FeO + Co \quad (3.3)$$

$$Fe + NiO \rightarrow FeO + Ni \quad (3.4)$$

As you proceed along the bottom of the Ellingham diagram, the oxygen affinity of the compound increases. At the heating point of glass-ceramic, iron has a stronger oxygen affinity than nickel and cobalt, as indicated in Figure 3.1. As a result, cobalt and nickel are mostly used to provide adhesive qualities [54, 67].

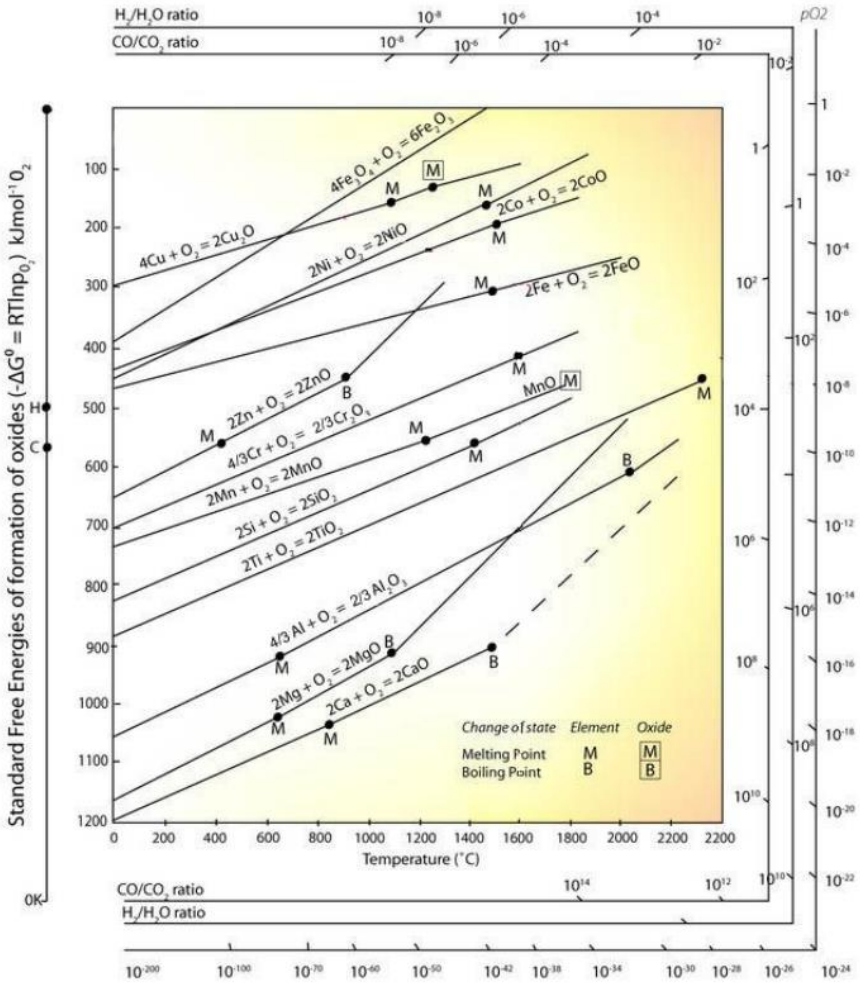

Figure 3.1 Ellingham Diagram [54]

3.3.3 Mechanical Theory

The mechanical approach is based on the field of contact between the substrate and the coating. [54]. Chemical (using hydrochloric HCl and sulfuric acid H_2SO_4) and mechanical treatment of the metallic substrate surface enhances the glass-ceramic/substrate contact [58].

3.4 Properties of Glass-Ceramic Coatings

3.4.1 Thermal Properties

3.4.1.1 Thermal Expansion

Thermal expansion occurs when the volume or length of a material increases as the temperature rises. In other words, the volume or length changes occurring in the substance can be determined by follow up them at 1 unit temperature change. The thermal expansion coefficient is calculated by multiplying the unit shape change by the temperature difference. The linear thermal expansion coefficient explains the change in the length of the material as the temperature of 1 °C rises. The following equation is used to calculate the linear thermal expansion coefficient (α):

$$\alpha = \frac{1}{l} \text{ x } \frac{\Delta l}{\Delta t} \tag{3.5}$$

where l is the length of the material, and Δl is the elongation obtained by means of heating through Δt °C.

The volume thermal expansion coefficient explains how the volume of a material changes as the temperature rises by 1 degree Celsius. In isotropic bodies, such as amorphous structures and glasses, the relationship between the volume thermal expansion coefficient (β) and the linear thermal expansion coefficient (α) is as follows:

$$\beta = 3 \, . \, \alpha \tag{3.6}$$

The thermal expansion coefficient in glass-ceramic coatings is important because it affects the bond between glass-ceramic coatings and metal. The thermal expansion coefficients of glass-ceramic coating and substrate metal must be close to each other in order for glass-ceramic coatings technology to work. The glass-ceramic coating will shrink quickly during cooling after firing if the thermal expansion coefficient of the glass-ceramic coatings is lower than that of metal. The metal surface stands out against glass-ceramic coating shrinkage when the glass-ceramic coating-metal bond is

particularly strong, as determined by glass-ceramic coatings adhesion parameters. Stress-developing cracks stay in the structure when the glass-ceramic coatings' tensile strength is surpassed in this case. Chipping defects, on the other hand, occur when the metal's thermal expansion coefficient is lower than glass-ceramic coatings' compressive strength. The expansion coefficient of the glass-ceramic coatings should be less than the metal in glass-ceramic coatings applications because compressive strength is 15-20 times more dangerous than tensile strength [68-69]. Table 3.3 lists the volume thermal expansion coefficients of a variety of metals and glass-ceramic coatings.

Table 3.3 Cubical thermal expansion coefficients of some glass-ceramic coatings and some metals [69]

Material	**Cubical Thermal Expansion Coefficient ($3.\alpha \times 10^{-7}$)**	**Temperature Range (°C)**
Iron	426	0 – 500
Low Carbon Steel	465	27 – 760
Cast Iron	378 – 390	20 – 500
Ground Coat for Steel	240 – 300	0 – 100
Cover Coat for Steel	280 – 360	0 – 100
Ground Coat for Cast Iron	250 – 300	0 – 100

3.4.1.2 Thermal Shock

The thermal shock resistance of glass-ceramic coatings describes how the glass-ceramic reacts to rapid temperature changes and is calculated mathematically according to Winkelmann and Schott's proposal:

$$K = \frac{P}{\alpha.E}\sqrt{\frac{\lambda}{c}.d} \tag{3.7}$$

where P is tensile strength, α is the linear expansion coefficient, E is the elasticity modulus, λ is the thermal conductivity coefficient, c is the specific heat and d is the density.

Thermal shock resistance is determined by a variety of factors, including not only specific thermal properties, but also a variety of other factors. Internal strains play the most important role here. Because glass-ceramic coatings have a lower coefficient of thermal expansion than metal, it creates compressive strains during rapid heating and tensile strains during rapid cooling. Because compressive forces are weaker than tensile forces, glass-ceramic coatings are more resistant to thermal shock during rapid heating. The magnitude of the strains is also important in this case. The thermal shock resistance of convex surfaces is lower than that of concave surfaces because convex surfaces have more tension than concave surfaces. Thermal shock resistance is also affected by glass-ceramic coating thickness and substrate metal thickness [68].

As previously stated, glass-ceramic coatings'' thermal shock resistance is reduced when they are rapidly cooled. The cooling environment, on the other hand, is crucial. The action of thermal shock with cold air is weaker than that of thermal shock with cold water. As a result, cold water tests are used to assess the thermal shock resistance of glass-ceramic coatings [70].

3.4.1.3 Fusibility and Fluidity

Fusibility and fluidity are important properties related to the molten state that come to the fore during the melting and firing of glass-ceramic coatings raw material after application. The chemical composition is in charge of it, but its calculation has largely remained experimental. The majority of the calculations were correct for a specific range of composition. As a result, tests like the cone fusion test, fusion flow test, fusion block test, bead test, and interferometer test have become important for each glass-ceramic coating composition. The cone fusion test determines deformation intervals, the fusion flow test determines temperature-related hardness and softness of frit, the fusion block test determines the fusion temperature of glass-ceramic coatings compositions, the bead test determines frit fusibility, fluidity, and surface tension properties, and the interferometer test determines the expansion coefficient [68].

3.4.1.4 Viscosity

The viscosity property of glass-ceramic coatings, like that of all glassy materials, is a valid parameter that is highly affected by temperature, so a small change in temperature can cause a large change in viscosity. T_G temperature is the temperature at which the material becomes brittle and has a viscosity of 1012 N.sec/m^2 as shown in Figure 3.2. The viscosity value was 10 N.sec/m^2, and the melting temperature was T_S.

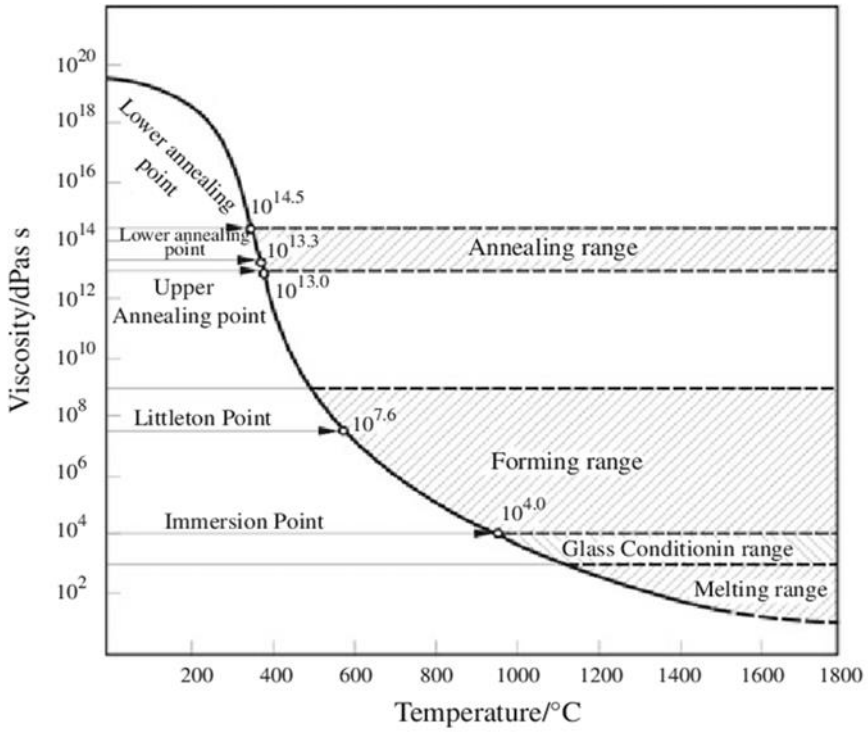

Figure 3.2 Viscosity – Temperature curve for a theoretical glass [71]

The chemical composition can be used to calculate these values. In glass-ceramic coatings, the T_G temperature is usually below 500 °C, and the T_S temperature is around 1400 °C. In addition, as the viscosity rises, the glass-ceramic coatings' firing temperature rises, the gas evolution decreases, and the surface flatness rises. Low viscosity values, on the other hand, cause glass-ceramic coating defects and uneven coating thickness. The viscosity of glass-ceramic coatings varies between 102 - 103 N.sec/m^2 during the firing process [68].

The viscosity values of the prepared glass-ceramic coating slurry can be easily adjusted in wet applications of the glass-ceramic coating process using materials such as boric acid, clay, and sodium nitrite.

3.4.2 Physical and Mechanical Properties

3.4.2.1 Density

In wet applications, the density (specific gravity) property is commonly used to control the fluidity of the sample. Glass-ceramic coatings should be diluted in terms of density, which can be measured with a pycnometer. The formula for calculating glass-ceramic coatings' density is:

$$S = (w - p)/[(w - p) - (w_2 - w_1)] \quad (3.8)$$

where S is the specific gravity of glass-ceramic coating, w is the weight of the tapered pycnometer and sample, w_1 is the weight of the tapered pycnometer filled with water, and w_2 is the weight of the tapered pycnometer, sample, and water, and p is the weight of the tapered pycnometer [69].

3.4.2.2 Specific Heat

The amount of heat required to raise the temperature of a 1 kg material at constant pressure and volume by 1° C is known as specific heat. The formula for calculating the specific heat of glass-ceramic coating is as follows:

$$S = p_1. s_1 + p_2. s_2 + p_3. s_3 \ldots \quad (3.9)$$

where S is the specific heat of the glass-ceramic coating, p is the percentage of the oxide and s is the factor for the oxide [69].

3.4.2.3 Hardness

Glass-ceramic coatings' hardness values vary little depending on chemical composition, and according to the Mohs scale, glass-ceramic coatings' hardness values range from 5 to 6. Rockwell, Brinell, and Knopp hardness measurement methods are not commonly used because they produce insufficient results for glass-ceramic coatings. The scratch resistance of glass-ceramic coating is also measured using the Mohs scale [69].

3.4.2.4 Elasticity

Despite the fact that elasticity is an important property in materials, it is not commonly used in the glass-ceramic coatings field. Mechanical and sonic methods can both be used to analyse it. The mathematical formula for the mechanical method is:

$$E = 4PL^3/bd^3\Delta \quad (3.10)$$

where P is the load, L is the length of the material, b is the width, d is the thickness and Δ is the deflection [69].

3.4.2.5 Compressive Strength

The compressive strength of glass-ceramic coatings is a frequently overlooked property that has the potential to influence other characteristics. For standard glass-ceramic coatings, it has a value of 77-81 kg/mm^2 and can be calculated using Winkelmann and Schott's formulas [69].

3.4.2.6 Tensile Strength

Although glass-ceramic coatings tensile strength is an important property, determining it can be difficult. Due to their brittle fracture properties, glass-ceramic coated materials are excellent for breaking. As a result, a variety of approaches to its examination have been proposed. Although it is not a desired or directly analysed property, it has an impact on the thermal properties of glass-ceramic coatings, particularly their thermal expansion [69].

3.4.3 Chemical Properties

3.4.3.1 Acid Resistance

Glass-ceramic coatings are constantly exposed to acid attack in a variety of applications, particularly in kitchenware. SiO_2 is one of the most important oxides affecting acid resistance because the acid resistance of the glass-ceramic coating is determined by the continuity of the structure $[SiO_4]$ in the glass-ceramic coatings. To resist the corrosive effect of acid, $[SiO_4]$ tetrahedrons are used to cover the surroundings of $\{[AlO_4] - R^+\}$ and $\{[BO_4] - R^+]\}$ in the structure. That is, as the SiO_2 content in the glass-ceramic coatings recipe rises, so does acid resistance. In contrast, as the R_2O group in the structure grows larger, the Si-R-O structure formed by ions like Li^+, Na^+, and K^+ disrupts the continuity of the $[SiO_4]$ tetrahedrons, lowering acid resistance. [72-73].

3.4.3.2 Alkali Resistance

Depending on the area of application, glass-ceramic coatings may also be subjected to an alkaline attack. The alkali attack, on the other hand, is slower than the acid attack. As a result, the glass-ceramic coatings' alkali tests are longer lasting. Furthermore, when corrosive materials that cause ion exchange leach in the coating structure are compared to acid and alkaline solutions, the effect of corrosive materials that cause ion exchange

leach in the glass-ceramic coatings structure is lower. Sodium pyrophosphate, sodium hydroxide, and sodium bicarbonate solutions are commonly used to test it.

The hydrogen ions in the solution react with the glass-ceramic coatings matrix and cause the alkaline ions in the glass-ceramic coatings to ionise, resulting in the ion exchange leach of glass-ceramic coatings. This is a pH-dependent reaction that occurs most often at pH <9 [73].

In the presence of two non-bridging oxygen atoms, the reaction between hydrogen ions and a silica network produces alkaline ions. This means that any of the alkali metal ions bound by non-bridged oxygen will easily replace hydrogen, resulting in the formation of an aqueous surface layer.

The dissolution of the silicate structure typically begins at pH > 8 and progresses as the pH rises. The OHs react with the hydrated layer or glass matrix at these pHs. The formation of Si(OH), the molecules that enter the alkaline solution, is the result of further reactions of hydroxyl groups with the first product. The second product, SiO^-, reacts with water to form $SiO^- + H_2O \rightarrow Si\text{-}OH + OH^-$ reaction. As a result of the repeated reactions with hydroxyl groups, glass-ceramic coatings is eroded [73].

3.4.3.3 Water Resistance

At room temperature, glass-ceramic coatings are resistant to water and retain their structural integrity. Furthermore, the coating structure is unaffected by hot water. The coating structure, on the other hand, begins to deteriorate after prolonged exposure to high temperatures and pressures at the point of use [73].

Glass-ceramic coatings in tests conducted according to the DIN EN ISO 4753-3 standard indicate that the glass-ceramic coatings should not exceed 8 mg/m^2 after 21 + 21 days (total 42 days) of testing [38]. In thermosiphon, valve, and boiler applications, water resistance is critical.

3.5 Application Areas of Glass-Ceramic Coatings

Glass-ceramic coatings possess superior engineering characteristics, such as resistance to high temperatures and chemical corrosion, as well as mechanical strength and aesthetic qualities, and can be found in a variety of applications, including water heaters, thermosiphons, boilers, fireplaces, pipelines, silos and hot water services. In addition to these properties, glass-ceramic coatings are a vital coating for kitchenware

and cookware because of their outstanding technical features, aesthetic appeal, and countless colour options [64, 65, 74].

3.6 Coating Methods for Glass-Ceramic Coatings

The wet and dry glass-ceramic coating processes are both available. The coating technique is chosen after considering the application area, cost, sheet metal properties, and glass-ceramic properties. Glass-ceramic coatings are glass-ceramic coatings that are applied to metal substrates.

3.6.1 Spraying Method

Spray glass-ceramic coating can be applied to body metal by compressing air and spraying glass-ceramic slurry or powder. Handwork spraying and automatic machine spraying are the two most common methods for spraying glass-ceramic coating. Automatic machine spraying allows for mass production [75].

For both indented and flat parts, spray glass-ceramic coating can be used. It's used in the manufacturing industry to cover stove side panels, kitchenware tools like pots and pans, kitchen trays, chassis, doors, body, grill, stove plate, and burner. Glass-ceramic slurry for spray glass-ceramic coating in the wet process should be optimal, meaning glass-ceramic suspension large enough to attach to the metal surface but small enough to pass through the spray nozzles, in order to achieve a better atomization effect. Batch particles larger than the nozzle diameter can clog the holes, resulting in no or intermittent glass ceramic application. This will slow down production and result in inefficient operations, as well as inhomogeneity in coating thickness and a rough coating surface. Aside from that, enough attention should be paid to the quality of the glass-ceramic surface after drying and firing to avoid cracking and shrinking [76].

The glass-ceramic powders spilled over the spray can be reused without adhering to the part, which is a significant advantage of the spray method. As a result, dust, oil, and dirt from the environment should be kept out of the cabin where the application is made [77].

Figure 3.3 Wet Spraying Method

3.6.2 Dipping Method

Dipping is the most basic and straightforward method of glass-ceramic coating. It's appropriate for single-color products. This method is commonly used to coat the inner and outer surfaces of pots and pans. If the metal body is small, round, and has a simple shape, all we have to do is dip it in batch and pull it out after it has coated enough batch, then turn, hook, or swing it to remove the excess batch.

The density of the batch in the immersion pool, the fineness of grinding, and the set value should all be monitored and controlled in order to achieve a uniform glass-ceramic coating [54].

Figure 3.4 Dipping Method in the Wet Process

3.6.3 Electrophoresis Method

Electrophoretic deposition (EPD) is a common technique for coating complex shapes in ceramics, such as the assembly of nanoscale particles into nanostructures and micropatterned thin films, solid oxide fuel cells, structural and functional composites, textured ceramics with crystalline oriented microstructures, and bio-compatible coatings on metal implants.

The density and particle size of the glass-ceramic, as well as the amount of power applied, are the most important parameters affecting coating quality in the electrophoresis method. There is a stable colloidal suspension with charged powder particles in this colloidal process. In this suspension, the depositing electrodes have the required shape. Electrophoresis and deposition are the two processes involved. The first step, electrophoresis, involves charged powder particles migrating towards an electrode under the influence of a DC electric field. Powder particles deposit on the dense mass electrode during deposition [78].

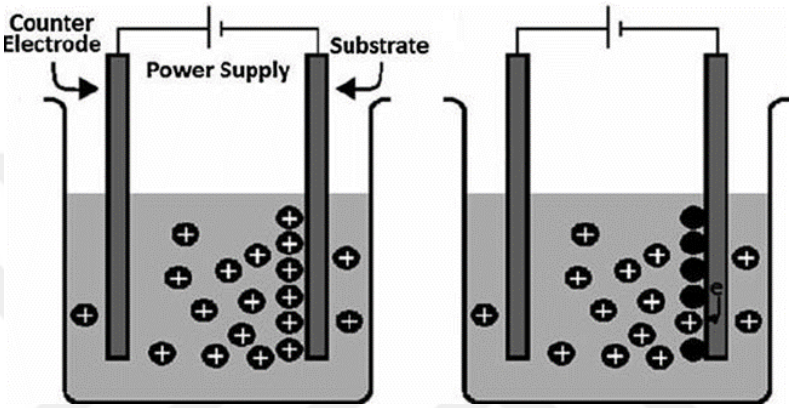

Figure 3.5 Electrophoresis and Deposition Process for Electrophoresis Method [79]

3.6.4 Flow Coating

The immersion method of the modern industry's modified version is called flow coating. The glass-ceramic-coated part isn't immersed in the batch in this method. Rather, one or two nozzles are used to pour the batch onto the part to be coated. This method is less expensive and quicker than immersion [54].

Figure 3.6 Flow Coating Method

3.6.5 Thermal Spray Method

Thermal spraying is a group of coating processes in which finely divided metallic or non-metallic materials are deposited in a molten or semi-molten state to form a coating. It entails injecting powder particles into a hot, high-velocity gas jet, where they are heated, accelerated, and projected onto a substrate to form a coating [80-81].

Plasma spraying, high-velocity oxy-fuel spraying, D-gun spraying, combustion flame spraying, and arc-wire spraying are some of the processes used [82].

In this method; between the substrate and the molten or semi-molten glass-ceramic particles, Van Der Waals forces, diffusion bonding, and mechanical bonding occur. Depending on the process and feedstock, the coating thickness ranges from 20 m to several mm. Electrical (plasma or arc) or combustion heating is used to heat the material (combustion flame). Thermal spraying methods have the disadvantage of producing high-porosity coatings. Due to the glass-ceramic composition, it has good adhesion, high hardness and density, and high corrosion, heat, and wear resistance [80].

3.6.6 Electrostatic Powder Glass-Ceramic Coating Method

The application of electrostatic coatings is based on the transfer of an electric charge to dry powder particles. Glass-ceramic in the form of solid powder is electrostatically charged with an applied voltage of about 80-100 kV and sprayed on the substrate material in this method. The charging electrode's supplying voltage and current have an impact on the coating quality. The powder can bond to the substrate material by adjusting the voltage settings [54-83].

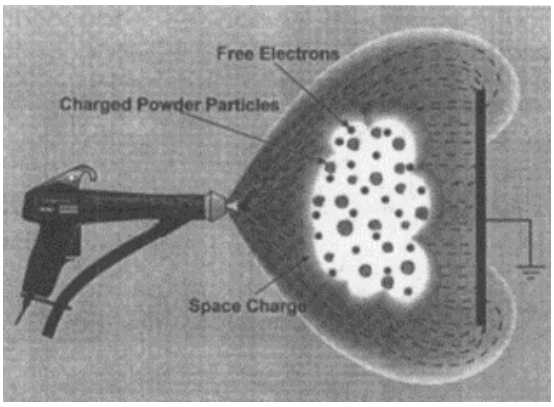

Figure 3.7 Charging of Powder Particle Particles in Corona Discharge

4
BLAST FURNACE SLAG

Iron and steel manufacturing plants are material-intensive industries that convert iron ore or iron scrap materials into steel within a day. These integrated plants are separated into two main production routes, iron ore, and iron scrap, according to the raw material used [84]. These plants are BF (Blast Furnace) - BOF (Basic Oxygen Furnace) plants that use iron ore as raw material, and EAF (Electric Arc Furnace) plants that use iron scrap as a raw material [84]. The first step in this refining and transformation manufacturing process takes place in a BF facility, which processes the raw materials to produce crude iron with a high carbon concentration (4-5 %C) [85].

4.1 Formation of Blast Furnace Slag

Blast Furnace Slag (BFS) is formed by smelting iron ore, iron scrap, coke, and flux during the ironmaking process. This pyrometallurgical method utilizes around 1400 kg of iron ore, 800 kg of coal, 300 kg of flux, and 120 kg of iron scrap to obtain 1000 kg of crude iron [85].

Iron ores are mainly extracted from rocks in the form of hematite (Fe_2O_3 ~ 70% Fe) or magnetite (Fe_3O_4 ~ 72% Fe) in the production of iron crude [86]. Coke, which has minimal impurities and a high carbon concentration, is utilized as a fuel and reducing agent in the BF process. Limestone and dolomite materials are used as a flux. These fluxes are sedimentary carbonate rocks made primarily of calcite ($CaCO_3$) and dolomite ($CaCO_3.MgCO_3$) [86]. The chemical composition of limestone and dolomite is given in Table 4.1 [86].

Table 4.1 Chemical composition of fluxes is used in ironmaking [86].

Component	**Limestone**	**Dolomite**
$CaCO_3$	95.3	54.5
$MgCO_3$	3.1	42.0
CaO	53.4	30.6
MgO	1.5	20.1
SiO_2	0.7	2.6
R_2O_3	0.3	0.3

Coke, iron ore along with flux, is first charged into the top of the BF. A hot air blast of around 1000 °C is injected from the furnace's base through nozzles called tuyeres [87]. The furnace's hot air blast to the furnace burns the coke resulting in CO (carbon monoxide). The hot air maintains the high temperatures required by reductant gases to convert the iron oxide in iron ore to iron [84]. In the BF, the fluxing agents (limestone and dolomite) fuse with the gangue (siliceous and aluminous residues from iron ore) and coke ash to obtain slag [88]. The slag is generated to make it easier to fusible the impurities in the raw materials, and it is a combination of these impurities. Iron ores exist in nature with the impure situation. The impurities extracted from the molten metal, combine with the basic oxides in the fluxes to form slag in the CaO-MgO–SiO_2-Na_2O-K_2O–Al_2O_3-Fe_2O_3 system, and the slag is eliminated from the furnace (Figure 4.1) [85]. Calcination of limestone begins at temperatures higher than 800 °C in the BF, and decomposition of dolomite begins at around 700 °C [86]. These decomposition processes are endothermic reactions. CaO (calcium oxide) has a base nature and reacts with acidic impurities in the iron ore. In addition, the sulphur in the various raw materials is absorbed by the liquid slag [86].

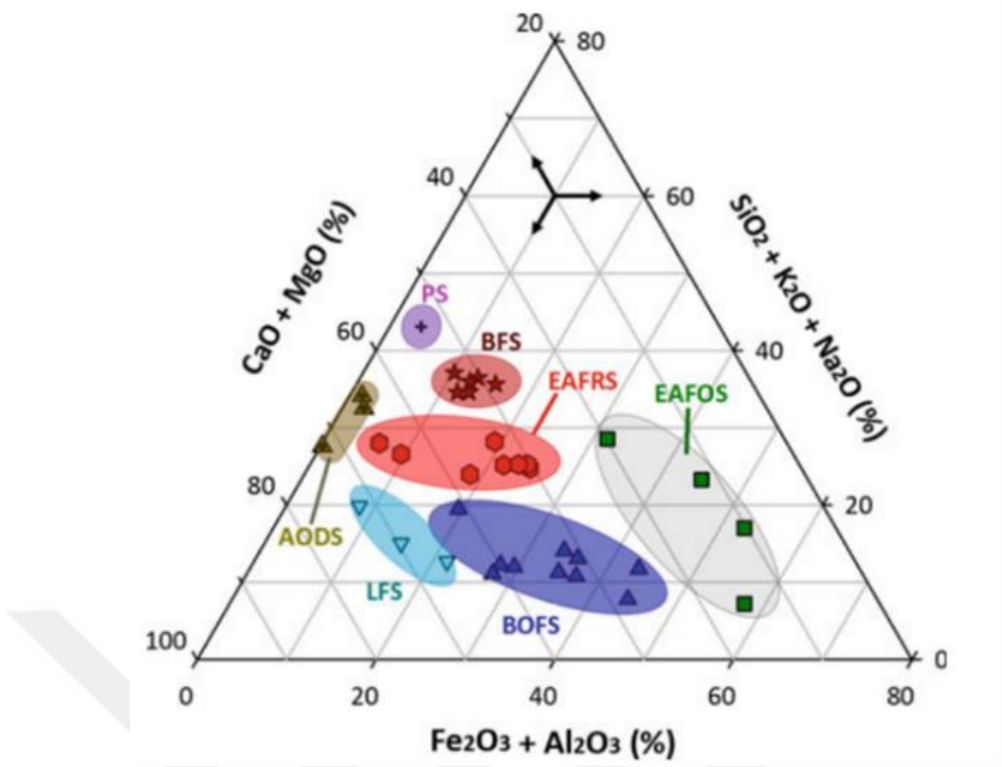

Figure 4.1 Normalized CaO (MgO)–SiO2(Na2O, K2O)– Al2O3(Fe2O3) phase diagram for various types of iron and steel slags. Acronyms: blast furnace slag (BFS); basic oxygen furnace slag (BOFS); electric arc furnace reducing slag (EAFRS); electric arc furnace oxidizing

4.2 Chemical Compositions of Blast Furnace Slag

Depending on the nature of the ore, the chemical composition of the fluxes, and coke consumption, the chemical composition of slag might vary significantly between operations [86]. These differences have an impact on the concentration of the four main ingredients, lime, silica, alumina, and magnesia, and the contents of the minor ingredients, sulphur, and manganese oxides. The chemical composition of BFS is given in Table 4.2.

Table 4.2 Chemical composition of Blast Furnace Slag

Reference	**SiO_2**	**Al_2O_3**	**Fe_2O_3**	**CaO**	**MgO**	**SO_3**	**TiO_2**	**MnO**
Japan [89]	33.8	13.4	0.4	41.7	7.4	0.8	-	0.3
India [90]	32.97	17.97	0.72	35.08	10.31	-	-	-
Australia[91]	34.4	14.5	-	40.5	6.5	-	1.5	0.5
Spain [92]	32.32	10.62	0.86	45.20	6.35	2.03	0.54	0.31
Poland [93]	38.7	7.7	0.6	40.5	6.32	0.31	-	-
Mexico [94]	32.3	10.5	0.5	39.4	8.7	3.2	-	0.5

4.3 Types of Blast Furnace Slag

In the reusing of BFS is generally based on cooling process. When the BFS is cooled, air-cooled, granulated, and pelletized or expanded types are obtained. Pelletized expanded slag is cooled by a water jet. Steam, and developing vesicles is obtained, hence the density of slag is reduced and leads to bind with hydraulic cement paste as a good mechanical bond [95]. This finely ground, expanded slag generally used as a lightweight aggregate and can possess similar cementitious properties with GGBFS [95]. BFS is divided into air-cooled BFS and granulated (crystallized) BFS, as shown in Figure 4.2.

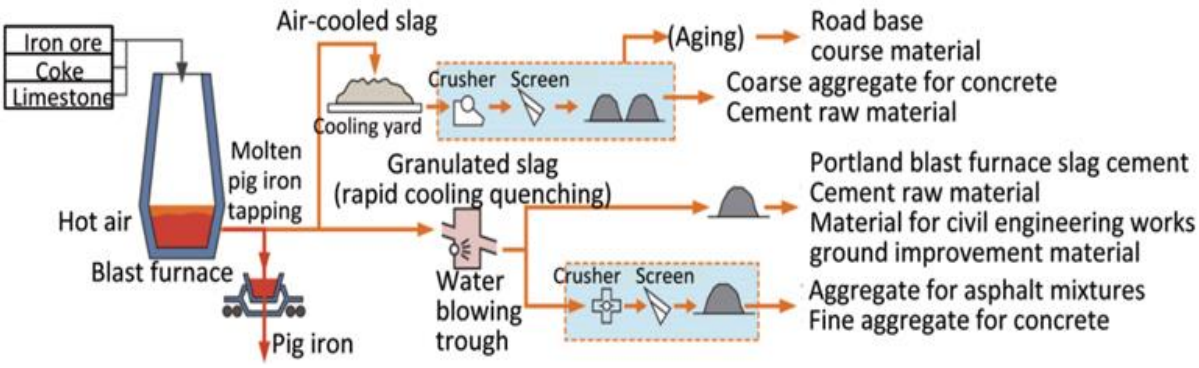

Figure 4.2 Production flow chart of Blast Furnace Slag

Air-cooled BFS is produced by allowing molten slag to cool in open pits or yards [87]. The rapid cooling of molten BFS with a high-pressure water jet produces granulated

blast-furnace slag (GBFS). This granulated slag contains glassy granular particles (≤ 5 mm) like sand [96]. Approximately 80% of BF slag is rapidly cooled from a molten state of about 1500 °C to glassy sand termed granulated slag [87]. The remaining 20% is cooled naturally or with water spray before solidifying into rock-like lumps. These lumps, known as air-cooled slag, are crushed, sieved, aged to prevent the environmental impact, and finally delivered as finished materials. The physical properties of air-cooled BF slag are given in Table 4.3.

Table 4.3 Physical properties of air-cooled Blast Furnace Slag [86].

Specific density	Bulk density (kg/m^3)	Water absorption (%)	Impact value dry (%)	Crushing value (%)	Polished stone value (%)	Abrasion value (%)
2.38–2.76	1150-1440	1.5–5	21–42	25–39	50–63	5–31

Air-cooled blast furnace slag has been extensively used as a construction aggregate and provides superior mechanical properties to aggregate slag concrete [97]. The granulated BFS can replace up to 50% clinker in the production of cement [98] owing to the excellent hydration properties of BFS. Granulated BFS allows for improving the resulting product qualities, reducing raw material and energy consumption, and decreasing the environmental impact of cement production [97]. The properties of ground granulated BFS are given in Table 4.4 [99].

Table 4.4 Physical properties of air-cooled Blast Furnace Slag [86]

Hydraulic Index	Bulk Density	Glass Content	Angle of Repose	Chloride Ion
1.7–1.9 %	850 kg/m^3	> 85%	Approx. 35°	< 0.025 %

The crystalline character of an air-cooled BF is due to gas bubbles dissolved in the molten slag, which result in a cellular or vesicular structure. The air-cooled slag is crushed to angular, roughly cubical particles with pitted surfaces [99]. Hydraulic cements or bituminous binder ingredients supply an excellent bond. High internal

friction angles and particle interlock lead to excellent stability. Bulk density is affected by particle size and grading; larger particles have more interior cells or vesicles and hence possesses a lower bulk density [99]. The coarse sizes may possess bulk densities as much as 20% lower than natural aggregates with the same gradation. On the other hand, the fine air-cooled BFS (passing a 4.75 mm or No. 4 sieve) is nearly equivalent density for natural sand [99]. Air-cooled BF slag possesses a low coefficient of thermal expansion and a high fire resistance. Air-cooled BFS possesses relatively high-water absorption because of its porosity [99]. BF slag is one of the more absorbent types of aggregates. The rough texture and relatively high porosity, together with its alkaline reactivity, generate excellent adhesive properties, especially in the presence of water [99].

4.4 Market Share of Blast Furnace Slag

The total worldwide production volume of pig iron increased from approximately 933 million metric tons in 2009 to 1.28 billion metric tons in 2019. Iron slag from blast furnaces may be estimated to be 25% to 30% of crude (pig) iron production [100]. The production quantity of BF slag is approximately 300 kg per ton of pig iron, and roughly 40 million tons of iron/steel slag is produced in Japan every year [87]. According to U.S. Geological Survey, world iron slag production was estimated to be between 340 million and 410 million tons in 2021 [100]. In 2021, Blast furnace slag was about 49% of the tonnage sold and accounted for 87% of the total value of slag, most of which was granulated in U.S. According to World Steel Association [101], 0.28 kg of BF slag is produced per kg of hot metal, and 97% of the total amount of BF slag generated is recovered, of which 84% is used for cement making. According to Eurofer [102], ferrous slag substituted in different production fields is shown in Figure 4.3 in 2020. The rise in total ferrous slag sales in 2018 was little greater than the increase in local cement sales [95]. GBFS sales increased by 0.3 million tons to 3.4 million tons in 2018, representing for 40% of BFS sales tonnages and 20% of total iron and steel slag sales tonnages. The overall value of GGBFS rose by $39 million to $345 million, accounting for 88% of BFS sales and 78% of total iron and steel slag sales [95].

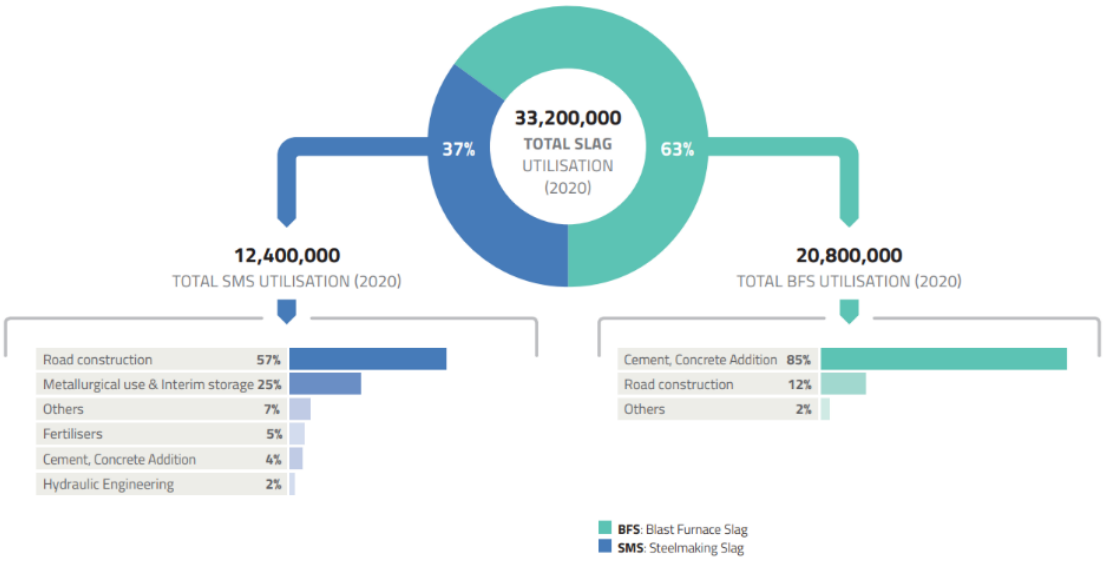

Figure 4.3 Total slag utilization [102]

4.5 Utilization of Blast Furnace Slag as an Alternative Raw Material

Utilization of the BFS creates benefits in respective engineering, economic, and environmental. It is significant that establish a relationship between the properties of the resultant product and the properties of slag such as mineral, chemical, physical, and even "negative" properties [103]. If the resulting product is technically safe, environmentally acceptable, and economically viable, the benefits will coexist and there will be a potential for use of the slag, as shown in Figure 4.4 [104].

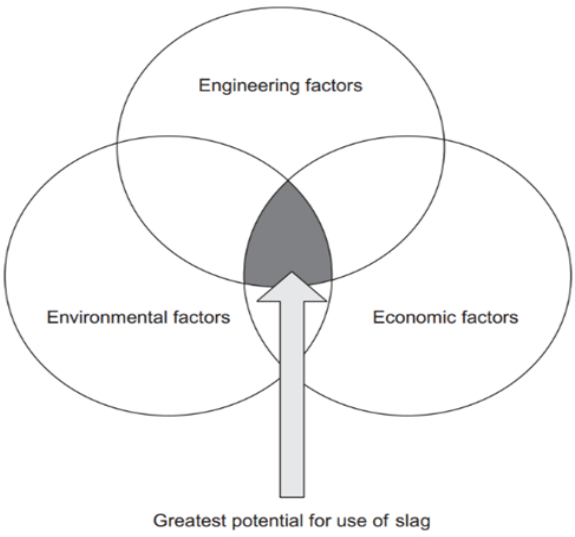

Figure 4.4 Sustainable key of utilization of slag [103]

4.5.1 Blast Furnace Slag as an Alternative Raw Material for Glass-Ceramics

Y. Fan et. al [105] investigated sintering mechanism, structure and crystallization of CaO-MgO-Al_2O_3-SiO_2 glass-ceramics from blast furnace slag with different amount ZnO. The resultant products were prepared by 60 wt. % BFS. SiO_2, Na_2O, K_2O, BaO, B_2O_3 and ZnO ingredients. The glasses or glass-ceramics were characterized by Raman Spectroscopy, Differential Scanning Calorimetry (DSC), Hot Stage Microscopy (HSM), XRD, and Field Emission Scanning Electron Microscopy (FE-SEM). The principal crystal phase of the glass-ceramics was akermanite ($Ca_2MgSi_2O_7$); ZnO promoted the precipitation of $Ca_2MgSi_2O_7$. With the increase in the ZnO content, the bulk density of the glass-ceramics increased while the flexural strength and microhardness decreased.

Y. Lui et. al [106] examined glass-ceramic glazes derived from blast furnace slag and fly ash. The total usage rate of industrial waste materials was 60 wt. %, some potash feldspar and borax additives were added as fluxing agents. The glass-ceramic glazes were characterized using Thermogravimetric Analysis (TGA), DTA, XRD and SEM devices. The anorthite ($CaAl_2Si_2O_8$) and akermanite ($Ca_2MgSi_2O_7$) crystalline phases were produced at 670 °C and crystallizing at 884 °C with disperse well in glassy matrix. The resultant crystalline phases can be obtained without further addition of nucleation agents due to existence of TiO_2 and Fe_2O_3 in the raw materials. This study demonstrates that BFS can be integrated into low-cost glass-ceramic glazes with economically and environmentally perspective.

L. Ding et. al [107] studied the impacts of various BFS contents on the microstructure, bulk density, water absorption, and bending strength of the glass–ceramic foams. Blast furnace slag (BFS) and waste glass were used as raw materials, with TiO_2, ZrO_2, and CaF_2 serving as nucleating agents, and $CaCO_3$, $Na_3PO_4.12H_2O$, and $Na_2B_4O_7.5H_2O$ serving as a foaming agent, a foaming stabilizer, and a flux agent, respectively. The major crystalline phases of the compositions are Diopside ($Ca(Mg, Al)(Si, Al)_2O_6$, Augite ($Ca(Mg, Al)(Si, Al)_2O_6$, and Titanite ($CaTiO(SiO_4)$. Usage of recycled BFS can lead create great economic and environmental benefits. The results showed that glass–ceramic foams with 50 wt. % BFS demonstrated excellent properties such as bulk density 0.79 g/cm^3, water absorption 2.71%, and bending strength 14.34 MPa.

4.5.2 Blast Furnace Slag as an Alternative Raw Material for Road Construction

Recycled materials used in construction can be classified according to three different source categories. These sources are industrial waste and/or by-products (mining waste rock, metallurgical slags, foundry sand, coal fly ash, municipal solid waste incinerator ash, etc.); another is road by-products, such as reclaimed concrete pavement materials, and finally reclaimed asphalt pavement materials; building demolition waste and/or by-products (crushed concrete, tiles, and bricks) [108]. Blast furnace slag are use in asphalt concrete as coarse aggregate, Portland cement concrete and granular base/sub-base material, binder in soil stabilization (ground slag). H. Quintana et. al evaluated warm mix asphalt manufactured with blast furnace slag [109]. Warm mix asphalt reduces the mixing and laying temperatures with respect to convectional mixtures of asphalt concrete in the asphalt. This decreases the energy is needed to produce asphalt mixtures and polluting emissions into the atmosphere [110]. Part of the coarse fraction of the natural aggregate was replaced by a BFS, advantages of using BFS in asphalt mixtures; they are materials with a rough and porous surface texture that can help improve adhesion with asphalt and increase skid resistance, good combability with asphalt, another is the improvements in resistance to moisture damage. In BFS composition, SiO_2 is related with high hardness and mechanical strength, and CaO leads to increase adhesion with asphalt and helps to enhance moisture damage resistance in asphalt mixtures.

4.5.3 Blast Furnace Slag as an Alternative Raw Material for Cement and Concrete

Rios et al. aimed to analyse the effects of replacing self-compacting concrete aggregates with air-cooled blast furnace slag. In the study, different mixes have been manufactured by substituting the fine and coarse natural aggregates by air-cooled blast furnace slag. The fracture energy and the tensile and compressive strength have been determined for each mix. The results show that the self-compactability of the concrete is gradually lost as the slag content is increased, thus, when the ratio of replacement is low, the concrete keeps the self-compacting properties. Also, the loss of self-compaction affected the mechanical properties by increasing its strength [111].

Qi et al. determined the adaptability of BFS in the production of concrete. They proved that the failure process of BFS concrete under compression was like that of conventional concrete [112].

In another study, Ulubeyli et al. investigated the recycling of the construction wastes (such as ceramic, brick, and marble) and BFS in the concrete together. According to the results, construction waste aggregates and BFS can be used to improve the mechanical properties, workability, and chemical resistance of the conventional concrete mixtures. Also, construction waste and BFS wastes are economically and environmentally suitable to use as aggregates in the production of more durable concrete mixtures [113].

Darshan et al. investigated the utilization of granulated BFS and cement in the manufacture of compressed stabilized earth blocks. Compression test and water absorption test were performed on the blocks. The test results showed that these blocks prepared with BFS, and cement can be utilized in masonry for load bearing wall construction [114].

Park, prepared calcium sulfoaluminate (CSA) cement with BFS or fly ash. The results obtained in this study provides that amorphous silica can stabilize in the blended systems at a very high degree of carbonation [115].

Liu et al. aimed to prepare of Eco-cement utilizing BFS, clinker and gypsum. Microstructural changes and hydration products of eco-cement were analysed with SEM and XRD. The results proved that it is feasible to use CFB fly ash along with BFS and clinker to produce Eco-cement [116].

Kanda et al. investigated medium volume BFS concrete. Combination of low shrinkage BFS and water curing was found to significantly strengthen shrinkage cracking resistance based the tests [117].

5
EXPERIMENTAL PROCEDURE

In this study, BFS is utilized as an alternative raw material in a glass-ceramic coating composition. 4% wt. of BFS is added to the composition as replacement of calcium carbonate ($CaCO_3$), quartz (SiO_2), alumina (Al_2O_3) and magnesium carbonate ($MgCO_3$) raw materials in the formulation. The experimental procedure consists of eight main steps: (i) Milling and sieving of BFS slag (ii) Characterization of BFS slag, (iii) Formulation, batch preparation and frits production, (iv) Characterization of frits denoted as F-STD and F-BFS, (v) Milling and sieving of the frits, (vi) Electrostatic application frit powders on metal substrates, (vii) Sintering and recrystallization of coatings denoted as GC-STD and GC-BFS, and (viii) Characterization of the glass-ceramic coatings. The glass-ceramic coating production procedures and the experimental flow chart are illustrated in Figure 5.1 and 5.2, respectively.

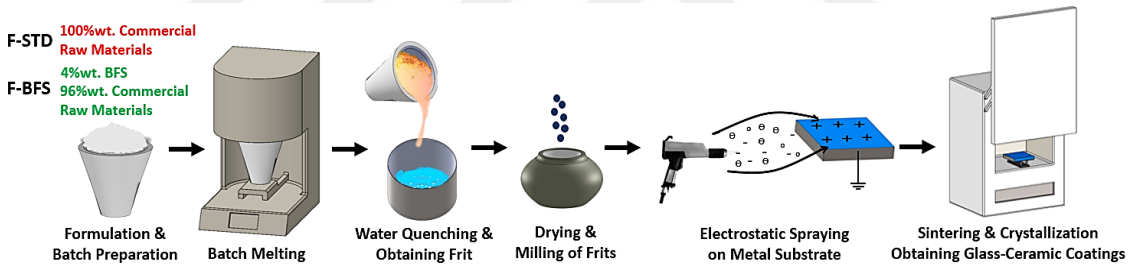

Figure 5.1 Glass-ceramic coating production procedure

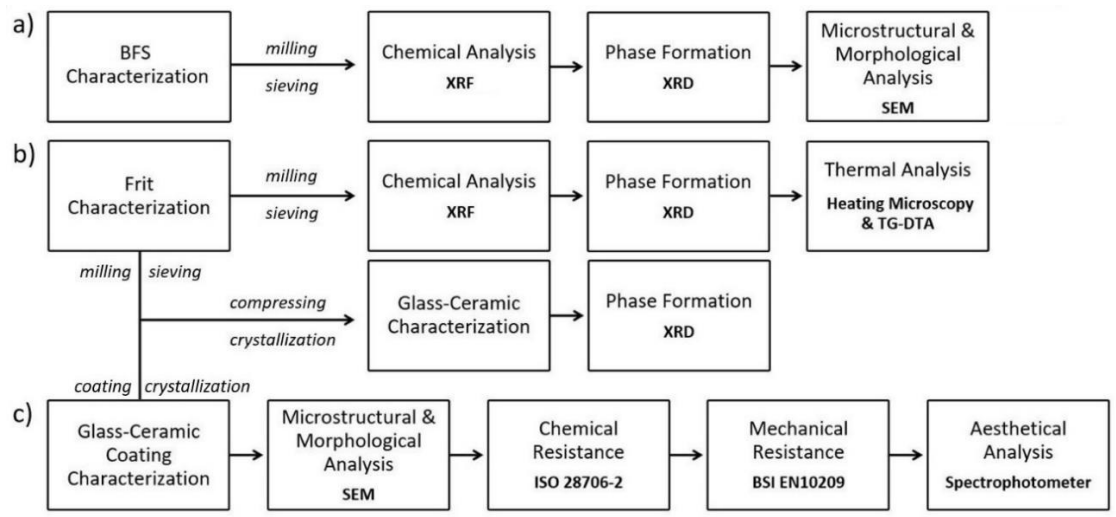

Figure 5.2 Experimental flow chart of the study

5.1 Materials

The required raw materials for the frit production which is the parent glass of the glass-ceramic coating were provided by Akcoat Advanced Coating Chemicals & Co.

Investigation of the utilization of BFS as a sustainable CaO, SiO_2, Al_2O_3, MgO etc. source to provide a circular production approach of glass-ceramic coating on steel substrate was conducted using the BFS waste supplied by Erdemir.

5.2 BFS Characterization

Before characterization of the BFS, it was dried in a pre-heat furnace at 300 °C and subsequently ground. The grinding procedure was conducted for 35 min using 800 g total alumina-zirconia balls in a ball mill, then sieved through 80 mesh (197 μm) sieves.

5.2.1 Chemical Analysis of BFS

X-Ray Fluorescence (Bruker AXS S8 Tiger XRF, Germany) analysis was operated to determine the chemical composition of BFS waste.

5.2.2 Crystalline Structure Analysis of BFS

X-Ray Diffraction analysis (Bruker XRD/D8 Advance, Germany- Cu K radiation, 40 kV, 25 mA, 2θ: 10 - 90°) was used to determine the crystallinity and crystal phases of BFS.

5.2.3 Microstructural Analysis of BFS

Scanning Electron Microscopy was operated to examine the microstructure and surface morphology of the BFS (SEM, Jeol JSM-6060LV, 20 kV, Japan).

5.3 Frit Preparation

According to the chemical and mechanical characteristics of BFS, the formulation of the glass-ceramic coating was calculated, then components in raw material batches were mixed and melted for 1 h at 1300 °C ± 100 °C. The molten glass was then rapidly cooled by quenching to produce frit, an amorphous glassy intermediate phase.

Chemical composition was obtained in the formation of the F-STD frit using 100% commercial raw materials such as quartz (SiO_2), soda ($NaHCO_3$), penta borax ($B_4H_{10}Na_2O_{12}$), aluminium oxide (Al_2O_3), calcium carbonate ($CaCO_3$), potassium nitrate (KNO_3), magnesium oxide (MgO), and others. 4 % wt. of the formulation BFS

was employed as sustainable CaO, SiO_2, AI_2O_3 and MgO sources and the 96 % wt. of the formulation commercial raw materials such as quartz (SiO_2), soda ($NaHCO_3$), penta borax ($B_4H_{10}Na_2O_{12}$), potassium nitrate (KNO_3) etc. were utilized to produce F-BFS.

5.4 Frit Characterization

5.4.1 Chemical Analysis of Frits

The chemical compositions of the frit powders were examined via XRF (Bruker AXS S8 Tiger, Germany). The lithium oxide (Li_2O) content of the frits were analysed using Atomic Absorption Spectrometry (PG Instrument PG-990 AAS, UK).

5.4.2 Crystalline Structure Analysis of Frits

To ensure that the frits are amorphous and to investigate the effect of BFS on the chemistry of F-STD and F-BOF frits were analysed by XRD (Bruker D8 Advance USA, Cu Kα radiation, 40 kV, 25 mA, 2θ: 5°- 85° with 0.02° step size).

5.4.3 Thermal Analysis of Frits

To determine the thermal behaviour of F-STD and F-BFS samples; $T_{Sintering}$, $T_{Softening}$, T_{Sphere}, $T_{HalfSphere}$ and $T_{Melting}$ temperatures were analysed by heating microscopy (Misura 3.32 ODTH HSM 1600-80, Italy). Thermal properties were examined up to 1250 °C with a heating rate of 10 °C/min up to 1250 °C due to geometric shape changes according to the DIN 51730 standards.

The coefficient of thermal expansion (COE) was measured in the range of 20 - 540 °C using a dilatometric device (DIL 402 PC Netzsch, Germany) with fused silica pushrod and sample holder, as well as a Pt–Pt/Rh thermocouple. The heating rate was 10 °C/min. For the preparation of dilatometer analysis, 5 × 5 × 25 mm piece of the sample was cut after pelletizing.

Thermal characteristics of the F-STD and F-BOF, and the effect of BFS on the thermal properties of the frits were investigated by Simultaneous Thermo Gravimetry-Differential Thermal Analysis (TG-DTA Netzsch STA 449F1A-0207-M, Germany). Weight changes occurring within F-STD and F-BOF were examined by thermogravimetry (TG) and enthalpy changes resulting from exothermic-endothermic reactions of glass-transition, crystallization temperatures etc. were performed by differential thermal analyses (DTA). Simultaneous TG-DTA analyses were conducted

to F-STD and F-BOF by using 30 mg of the frit powders in alumina crucible heated up to 1200 °C at constant 10 °C/min in heat flow in nitrogen (N_2) atmosphere.

5.5 Glass-Ceramic Coating Preparation

After drying of F-STD and F-BFS granules achieving with the quenching procedure, milling processes were applied to obtain powder form from frit granules by using a ball mill in 300 g frit granules with 750 g alumina-zirconia balls of 1 - 1.5 cm in diameter at 300 rpm for 25 min. At this stage, 1 ml silicone oil (C_2H_6OSi) was added to the mills, therefore electrostatic capability was achieved to prepare powders for electrostatic application.

The obtained frit powders were sieved through 80 mesh (197 μm) sieves. On a 10 x 30 cm DC01EK (EN10027-1) low carbon steel plate, pre-characterized F-STD and FBFS powders were electrostatically coated using electrostatic spray method with 150 - 200 μm thickness.

The coated plates were treated to sinter-crystallization processes to achieve a glass-ceramic coating on steel substrates. Preheating at 550 °C for 4.5 min (Protherm - PLF110/30, Turkey) and devitrification at 830 °C for 4.5 min (Protherm - PLF110/30, Turkey) were conducted to simulate the heating curve of commercial glass-ceramic coating manufacturing.

5.6 Glass-Ceramic Coating Characterization

5.6.1 Microstructural Analysis of Glass-Ceramic Coatings

SEM with an energy dispersive X-ray spectrometer (EDS) attachment was utilized to analyse the surface properties of the glass ceramic coated plates, including microstructure, surface morphology and surface chemical uniformity. The backscatter electron mode (BSE) was conducted for SEM and SEM-EDS studies, using a 15 kV acceleration voltage and a 9.5 mm operating distance.

GC-STD and GC-BFS surfaces were etched in 30 % wt. hydrogen fluoride (HF) solution for 3 min. Crystal structure that remains only on the surface after the corrosion of the glass by treating HF were inspected under SEM with an EDS attachment for further analysis and imaging of the crystal structure and crystalline morphologies of coatings.

1 x 1 cm of GC-STD and GC-BFS plates were mounted in a hot bakelite mold (Struers CitoPress, USA) and polished with an automatic polishing method (Struers Tegramin, USA). After the preparation of glass ceramic coating samples, SEM (Jeol JSM-6060LV, Japan) analyse was performed to cross-section between the coatings and the steel substrate in the BSE mode and microstructure of the glass ceramic coatings was examined. The adhesion mechanism between glass-ceramic and steel substrate was investigated.

5.6.2 Crystalline Structure Analysis of Glass-Ceramic Coatings

Crystal formation, phase analysis and amorphous structure of glass ceramic coatings were determined using XRD. Bulk glass ceramic coating samples were manufactured as follows for XRD measurements to detect the crystalline structure: 15 g frit was combined with 1 cc isopropyl alcohol (IPA) and formed into pellets with pressure, which were sintered at 830 °C for 4.5 min. The sinter-crystallized pellets were pulverized after the glass ceramic structures crystallized in order to undertake XRD measurements (Bruker D8 Advance USA, Cu Kα radiation, 40 kV, 25 mA, 2θ: 5°- 85° with 0.02° step size).

5.6.3 Thickness Analysis of Glass-Ceramic Coatings

The coating thickness of the coatings was measured with a DeFelsko Positest DFT Combo model coating thickness gage in order to examine homogenous coating distribution after electrostatic coating and sinter-crystallization to produce glass-ceramic coating according to ISO 2178:2016 standard. Coating homogeneity is a significant parameter in achieving good engineering properties such as adhesion, chemical resistance, etc. as well as maintaining these capabilities across the macro- and microstructure of coatings.

5.6.4 Adhesion Behaviour Analysis of Glass-Ceramic Coatings

The adhesion behaviour of glass-ceramic coatings can be examined by applying an impact resistance test. Adhesion behaviour was determined by dropping a 22 mm diameter cylinder apparatus weighing 1.5 kg from a height of 75 cm onto a glass-ceramic coated steel substrate, as described in the BS EN ISO 10209: 2013 standard. As a result, the impact of a 15 kJ energy on the coated surface was investigated using the standard. Impact marks on the coatings after applying impacts were interpreted according to ratings varying from 1 (optimum adherence) to 5 (failed adherence).

5.6.5 Chemical Corrosion Analysis of Glass-Ceramic Coatings

To assess the chemical corrosion resistance of the glass-ceramic coatings, a cold citric acid resistance test was conducted according to ISO 28706-1 standard. 10 g citric acid monohydrate ($C_6H_8O_7.H_2O$) and 100 mL distilled water (H_2O) are combined to prepare a solution. 4 mL of the solution is poured on the glass-ceramic coating surfaces at room temperature. To avoid evaporation of the solution, the acid-treated area of the surfaces was covered with a cap and let to stand for 15 min. After that, the plate was cleaned with water and dried. A pencil line was drawn over the region where the acid test was applied to grade the cold citric acid test. The AA in the test result represents the optimum acid resistance, while D denotes a failure.

Boiling citric acid tests were performed according to ISO 28706-2 standards to measure element migration and chemical corrosion resistance of glass ceramic coatings. A solution of 32 g pure crystalline citric acid monohydrate ($C_6H_8O_7.H_2O$) in 500 ml distilled water (H_2O) was applied to the glass ceramic coating surfaces at 95 °C for 2.5 h for the boiling citric acid test. After boiling citric acid treatment, the GC-STD and GC-BFS coatings were washed and dried. Weighing the coatings before and after the boiling citric acid test to quantify the corrosion amount of coatings indicated the weight loss. In addition to that, the solutions that were treated to coating surfaces for 2.5 h were taken. The solutions were subjected to Inductively Coupled Plasma Mass Spectrometry (Thermo Scientific X Series 2 ICP, USA) analysis to determine the amount of element migration from the glass ceramic coating to the boiling citric acid solution and the chemical corrosion resistance of the coatings.

5.6.6 Colour Analysis of Glass-Ceramic Coatings

A spectrophotometer (Spectrophotometer CM-700d, Konica Minolta) was utilized to perform colour analysis according to ISO 7724 standards and SCE D65 procedures. Colour values of the GC-STD and GC-BFS were measured in terms of L*, a*, and b*. The measured L value represents to lightness; a value represents to chromatic colour from red to green; b value represents to yellow to a blue chromatic colour value.

5.6.7 Gloss Analysis of Glass-Ceramic Coatings

Gloss is measured in five distinct spots at 60° using the TQC Sheen Polygloss glossmeter instrument. The figures represent the average of five measurements. A value

of 0 indicates the maximum opacity and a value of 90 denotes the maximum brightness of coatings.

6
RESULTS AND DISCUSSION

6.1 BFS Characterization

Table 6.1 shows the chemical composition of the BFS sustainable raw material as determined by XRF analysis. CaO, SiO_2, Al_2O_3 and MgO are the primary components of BFS, with B_2O_3, TiO_2, Na_2O, K_2O, MnO, Fe_2O_3, BaO, and SO_3 are the minor components. The chemical composition of the BFS waste was identical to that of instances seen in the literature. The chemical composition of BFS proved it appropriate to be utilized in frit, a precursor glass raw material, as a sustainable raw material source.

Table 6.1 Chemical composition of Blast Furnace Slag

Chemical Composition	% Wt.
CaO	44.12
SiO_2	29.16
Al_2O_3	12.80
MgO	5.29
B_2O_3	3.30
TiO_2	1.80
Na_2O	0.33
K_2O	0.51
MnO	0.37
Fe_2O_3	0.25
BaO	0.17
SO_3	1.87

The BFS x-ray diffraction pattern was shown in Figure 6.1 from 2θ: 10° to 2θ: 70°. The broad peak in the XRD patterns around diffraction angles 2θ: 25° - 40° indicated a degree of amorphous structure. There were also seen the gehlenite-akermanite crystal. Melilite group crystals, which are solid solutions of akermanite ($Ca_2Mg\ [Si_2O_7]$) and gehlenite ($Ca_2Al\ [Si_2O_7]$) have distinctive peaks about 2θ: 30° [19].

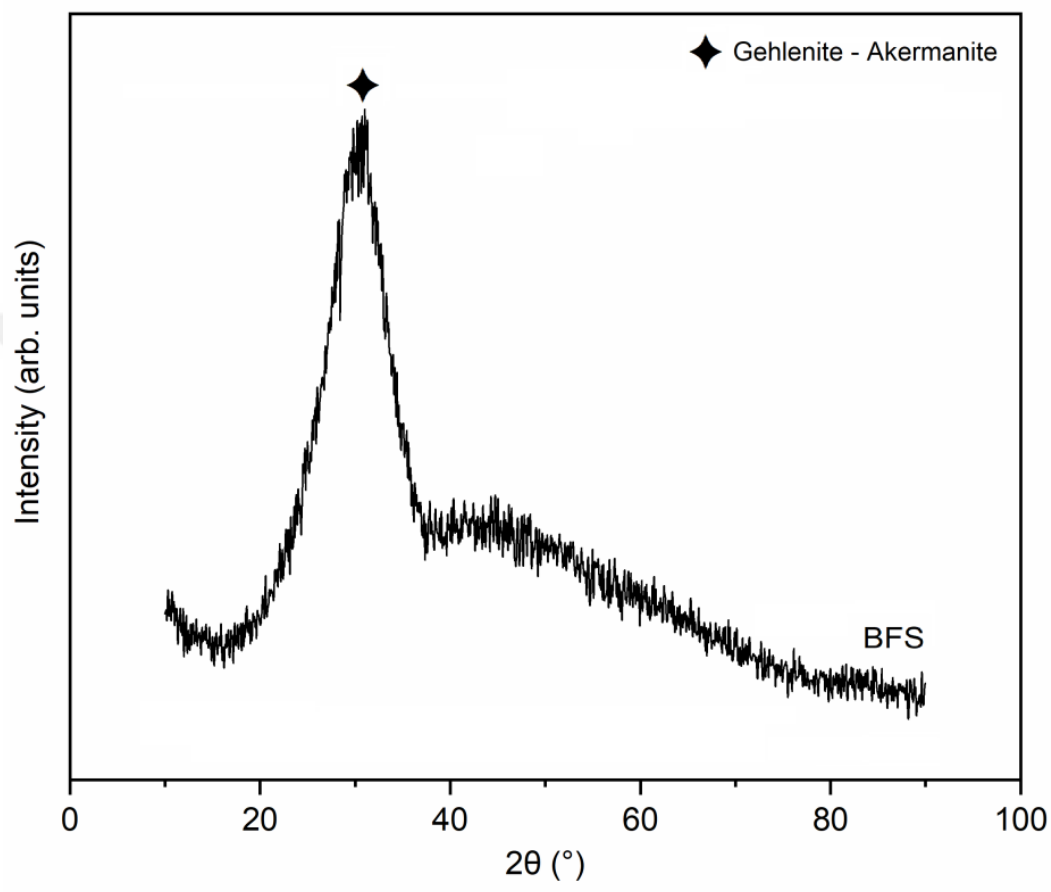

Figure 6.1 X-ray diffraction pattern of Blast Furnace Slag

Secondary electron yield imaging (SEI) mode was performed to capture SEM images. The image contrast in SEI mode is primarily determined by the sample surface morphology and texture. As illustrated in Figure 6.2, SEM images revealed that BFS had a compact particle morphology with various particle sizes ranging from 3–6 μm. The BFS particles have a rough surface texture with angular shapes and sharp edges that were obviously noticeable.

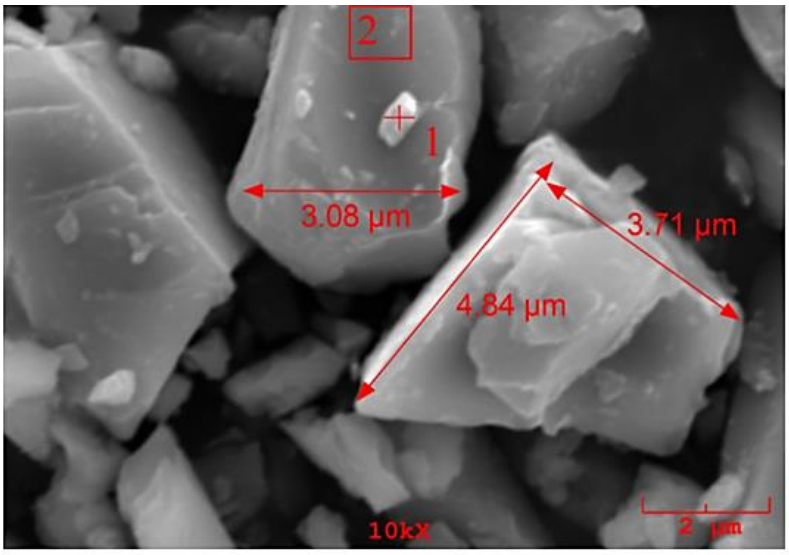

Figure 6.2 SEM image of Blast Furnace Slag

To examine the microstructure and elemental analysis, the EDS line spectrum of the BFS was evaluated in backscattered electron (BSE) mode from two different sites denoted as 1 and 2. The point 1 and region 2 were examined at Figure 6.3 and 6.4, respectively. The primary elements were oxygen (O), silicon (Si), and calcium (Ca), with a slight amount of aluminium (Al) and magnesium (Mg). In terms of chemical composition, the SEM findings were correlated with the XRF and XRD findings. There were also examined sodium (Na), sulphur (S), potassium (K) and titanium (Ti) as minor impurities of BFS.

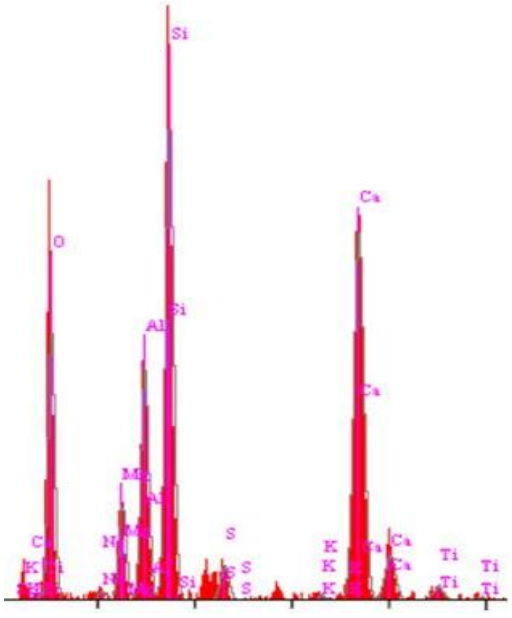

Element	Concentration %wt.
O	39.408
Na	0.487
Mg	3.673
Al	8.789
Si	19.365
S	1.625
K	0.263
Ca	25.094
Ti	1.296

Figure 6.3 EDS analysis result of Blast Furnace Slag pointed as 1

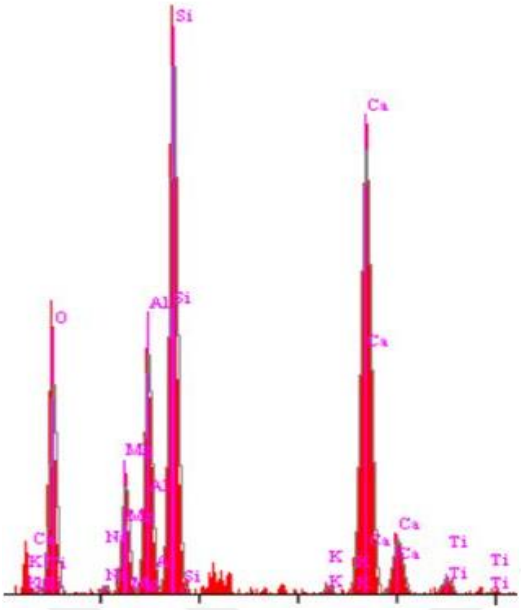

Element	Concentration %wt.
O	33.701
Na	0.434
Mg	4.155
Al	8.953
Si	21.224
K	0.418
Ca	29.673
Ti	1.443

Figure 6.4 EDS analysis result of Blast Furnace Slag pointed as 2

6.2 Frit Characterization

The chemical content of the frits F-STD and F-BFS were investigated utilizing XRF analysis present in the Table 6.2. The similarity of the chemical compositions of the sustainably produced F-BFS using 4 % wt. BFS combined with commercial raw materials and F-STD totally produced using commercial raw materials with SiO_2-B_2O_3-Na_2O-Al_2O_3-K_2O-F glass ceramic systems was confirmed. It indicated that the BFS can be an appropriate raw material source for CaO, SiO_2, Al_2O_3 and MgO etc. for the sustainable production approach on glass ceramic coating. The raw material replacement of BFS with commercial raw materials was achieved.

Table 6.2 Chemical content of the commercially produced F-STD and 4 % wt. sustainably produced F-BFS

		F-STD	F-BFS
	SiO_2	52.43	52.69
	CaO, Al_2O_3	5.05	4.97
R_2O	Na_2O, K_2O, Li_2O	13.94	13.97
RO	ZnO, MgO, BaO, NiO, CoO, MnO	5.41	5.61
R_2O_3	B_2O_3, Fe_2O_3	16.12	15.76
RO_2	TiO_2, ZrO_2	3.97	4.00
R_2O_5	P_2O_5	0.53	0.53
R	F	2.42	2.34

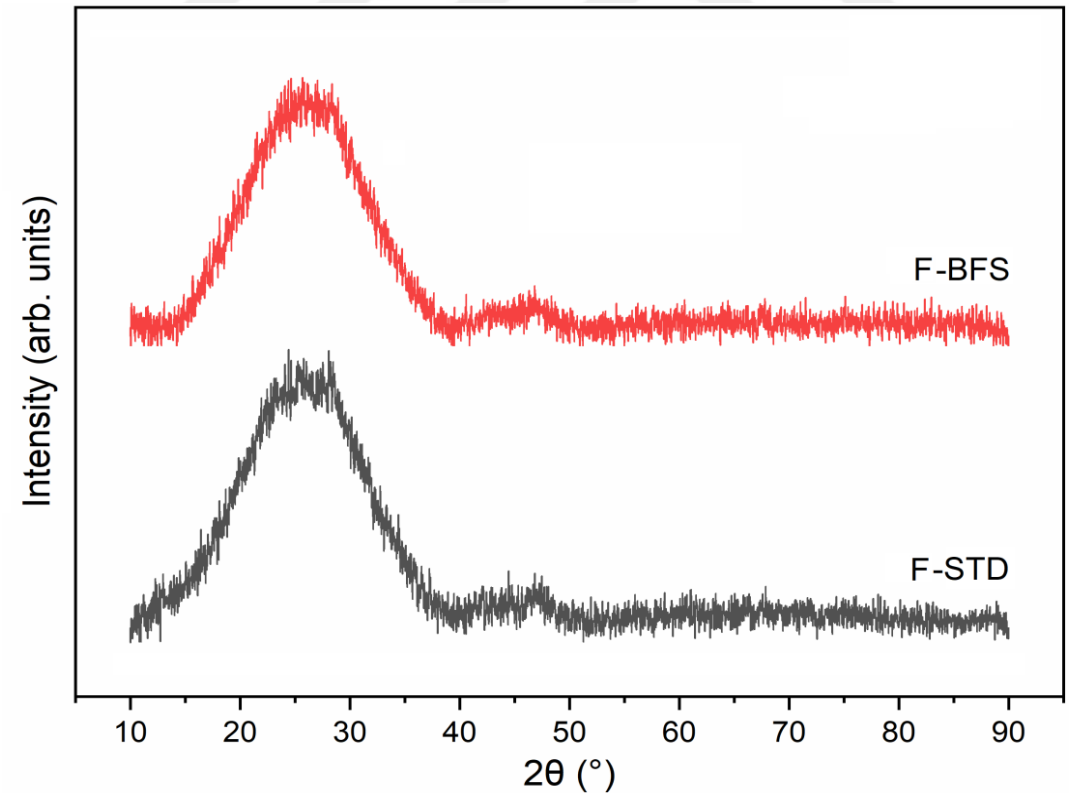

Figure 6.5 X-ray diffractometry patterns of F-STD and F-BFS

For F-STD and F-BFS, glass precursors, x-ray diffractometry patterns were demonstrated in Figure 6.5 from 2θ: 10° to 2θ: 90°. The broad peak between 2θ: 15°-35° was attributed to the amorphous structure, i.e. glassy phase. There was no prominent crystalline peaks in the patterns, meant both of frits had amorphous structure and quality quenching processes were conducted. F-STD was 73.5% amorphous, while F-BFS was 75% amorphous, according to qualitative XRD crystallinity measurements. Although no obvious peaks indicating the crystal phases were identified, the existence of crystal nuclei incorporated in the glass matrix is considerable to attribute for the qualitative crystallinity of 26.5 % for F-STD and 24.8 % for F-BFS.

	Sintering	Softening	Sphere	Half Sphere	Melting
F-STD	580	730	784	804	826
F-BFS	584	730	782	808	826

Figure 6.6 Heating microscopy results of F-STD and F-BFS

Prepared frits were subjected to heating microscopy analysis to examine the thermal behaviour, hereby geometric changes such as the height, width, and shape factor of the F-STD and F-BFS at different temperatures were evaluated. Heating microscopy analysis provides five characteristic temperatures. As demonstrated in Figure 6.6, according to the DIN 51730 standard, the first shrinkage with a 5%-dimensional change and the maximum shrinkage where rounded edges appear are named as sintering ($T_{Sintering}$) and softening ($T_{Softening}$) temperatures, respectively. The ball point where the first signal of melting appears, and the corners of the sample are completely round is identified as sphere temperature (T_{Sphere}). The half ball point where the sample height is half its base width and shape factor of at least 0.98 is the half sphere temperature ($T_{HalfSphere}$); the flow point where the sample melts and collapses to a third of its height at the hemisphere state is labelled as melting temperature ($T_{Melting}$) [118].

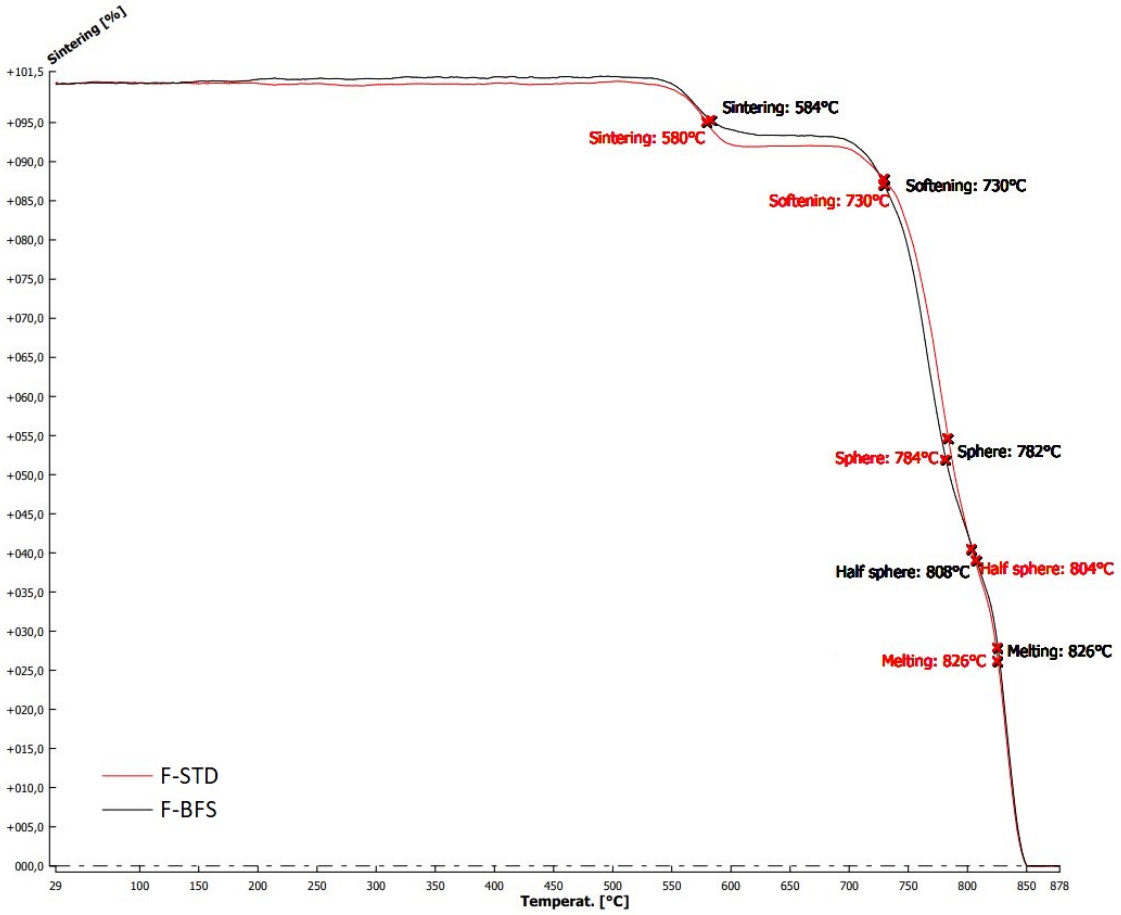

Figure 6.7 Heating microscopy curves of F-STD and F-BFS

The temperatures for $T_{Sintering}$, $T_{Softening}$, T_{Sphere}, $T_{HalfSphere}$, and $T_{Melting}$ were practically identical for the two samples, as shown in Figure 6.6 and 6.7. The sintering and half-sphere temperatures of F-BFS were slightly higher than those of F-STD, according to the heating microscopy measurements. Furthermore, F-BFS had a negligibly lower (2 °C) sphere temperature than F-STD. The viscous flow activation threshold is exceeded as the temperature goes up, and the material undergoes the sintering phase [21]. Because of viscous flow activation threshold of F-BFS is larger, the modest variation in $T_{Sintering}$ for the frit samples can be explained.

The F-BFS sample has a higher viscosity than the F-STD, as evidenced by the glass-transition temperatures (T_G) in the TG-DTA diagram in Figure 6.9 and the bubble formation mechanism apparent in the SEM image displaying in Figure 6.15. Equivalent $T_{Softening}$ values of F-STD and F-BFS implied that they have the identical maximum density, as expected given the same chemical content of F-STD and F-BFS regarding

the XRF analysis, as indicated in Table 6.2. At T_{Sphere}, F-STD and F-BFS were almost exclusively consist of liquid phases. At the time of sphere formation, T_{Sphere} was recorded. It was driven by the shape and surface tension of samples. F-BFS has a slight lower T_{Sphere} than the reference F-STD, which can be attributed to low surface tension induced by higher density and viscosity [21]. As can be displayed from the TG-DTA analysis in Figure 6.9, the minor changes in $T_{HalfSphere}$ between F-BFS and F-STD are due to minor differences in crystallinity and early crystallization of the fluorapatite phase in the reference F-STD. $T_{Melting}$ of both frits had an identical value.

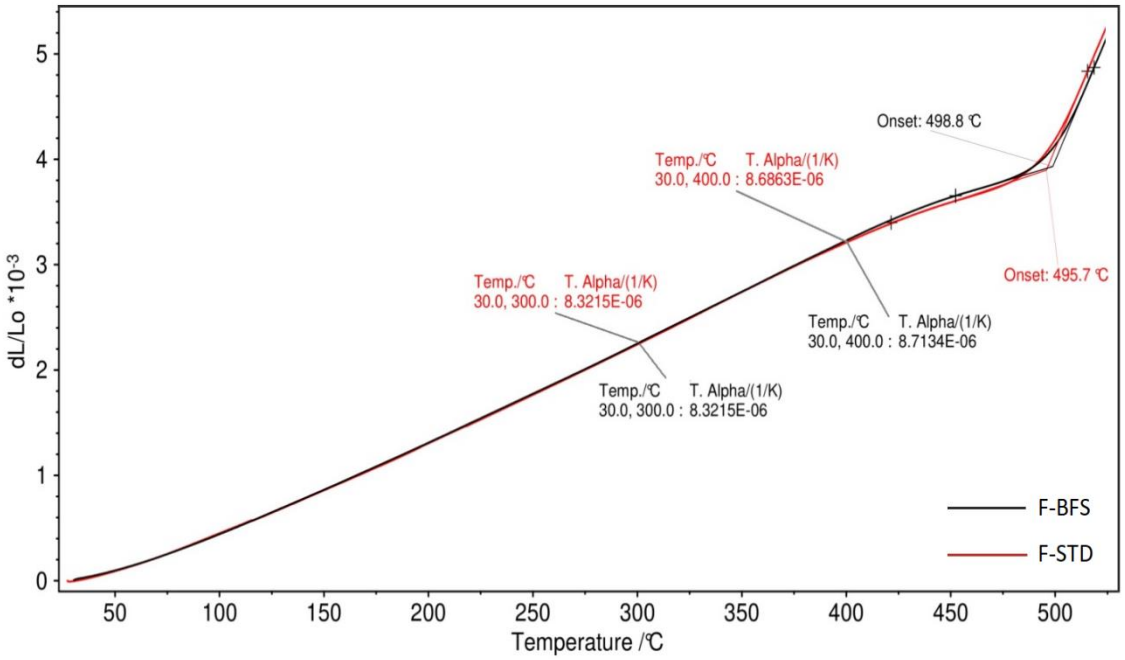

Figure 6.8 Dilatometric analysis of F-STD and F-BFS

Thermal expansion is the increase in body length or volume of the sample (F-STD and F-BFS) during heating. The linear coefficient of thermal expansion (COE) "α" is explained as the relative increase in length of a material sample as the temperature increases by one degree. The linear COE of the material is calculated with the equation given below.

$$\alpha = (1 / l) \times (\Delta l / \Delta t) \quad (6.1)$$

The change in body volume during heating up to 1 °C is called volumetric thermal expansion, shown as "β". For isotropic amorphous structures, the volume COE can be explained with sufficient accuracy by the following equation [15].

$$\beta = 3.\alpha \quad (6.2)$$

Achieving a strong bond and adhesion between glass-ceramic coating and steel substrate depends on the thermal expansion behaviour of the parent glass, i.e. frit. Glass-ceramic coating can only be obtained in an error-free way if the COEs of frits and the steel substrate are very close to each other [22].

When the tensile strength of the glass-ceramic coating is exceeded, cracks that cause tension in the structure are observed. On the other hand, when the COE of the metal substrate is much lower than the glass-ceramic, only chipping defects occur because the compressive strength of the glass-ceramic coating is higher. In glass-ceramic coating applications, the COE of glass-ceramic coating is always lower than that of metal substrate, as it is known that compressive strength is far more dangerous than tensile strength [69].

The thermal expansion coefficients, i.e. α values, of the F-STD and F-BFS were examined from room temperature to 550 °C. α values were measured at 300 °C and 400 °C temperatures. In Figure 6.8, these values are $8.32.10^{-6}$/K, $8.32.10^{-6}$/K for F-STD and F-BFS at 300 °C, respectively; at 400 °C, it was seen that it is $8.68.10^{-6}$/K and $8.71.10^{-6}$/K, respectively. Because of the high refractoriness, complex chemical composition, and compact structure of the BFS, glass ceramic with BFS substitution requires more energy to form amorphous structure. It appeared that the thermal characteristics of the frits were retained.

T_G temperature was also observed with this analysis. For supercooled liquids, it has been known in the literature that the T_G, expressed in absolute degrees, is approximately two-thirds of the melting point (T_M), i.e. $T_G / T_M = 2/3$ [119]. As can be seen in Figure 6.9, the T_G temperature of F-STD and F-BFS samples are 495.7 °C and 498.8 °C, respectively. In this analysis, which confirms that the characteristic temperatures of the samples seen in the heating microscopy are the similar, it is seen that the T_G increased only 3.1 °C, and it was attributed that the BFS embedded in the structure hardens the structure at a negligible level.

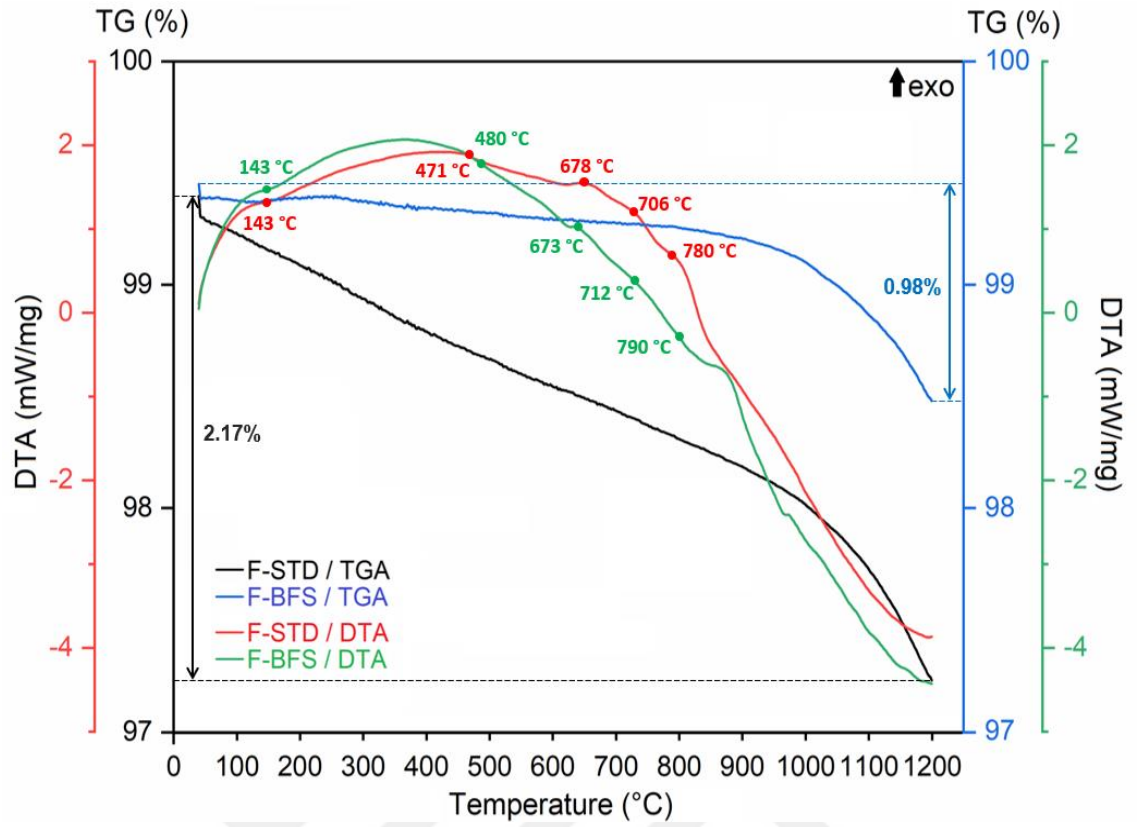

Figure 6.9 TG-DTA analysis of F-STD and F-BFS

Figure 6.9 illustrates the TG-DTA patterns of the reference frit F-STD and the sustainably manufactured F-BFS. The weight changes of the frits due to water loss, impurities removal etc. with temperature variations were examined employing thermogravimetry analysis (TGA). Differential thermal analysis (DTA) was conducted to understand temperature alterations caused by endothermic-exothermic reactions such as crystallization, decomposition and structural transformations etc.

The endothermic peaks in the DTA pattern of F-STD and F-BFS detected at 143 °C can indicate moisture, absorbed water, and impurities volatilization.

A shift in the baseline at approximately 475 °C could attribute to T_G. Even though there was no noticeable indicator of T_G in the DTA pattern, by calculating the first derivative of the pattern baseline the peak could be examined clearly. T_G of F-BFS observed at higher temperatures than T_G of F-STD, as shown in Figure 6.9. The decrease in fluorine (F) content in F-BFS (F-2.34 %wt.) compared to F-STD (F-2.42 %wt.), as determined by XRF analysis of the frits, was obviously the explanation of the reasonably high T_G of F-BFS. The viscosity of the glass system affects T_G, which is determined by the glass structure [23]. When fluorine is included into the glass structure, one Si-O-Si bond is

reconstructed by two Si-F bonds. The glass network is disrupted at Si–F, enables the viscosity and T_G of the glasses to decline [24].

The DTA curves of F-STD and F-BFS showed exothermic peaks at 678 °C and 673 °C, respectively, corresponding to the first crystallization temperature, T_{C1} which could be considered as the crystallization of the fluorine mica phase. At temperatures of (T_{C2}) 706°C and 712 °C, respectively, the second crystallization peaks of F-STD and F-BFS were identified, which were not easily noticeable in the DTA baseline, specifically in the case of F-BFS. At 780 °C and 790 °C, the final crystallization temperatures (T_{C3}) were detected in the curves. With increasing temperature, the relationship between temperature and the crystal formation behaviour of the frits evolved. For the chemical transformation and crystalline phase formation, frit generated from BFS required more energy than the F-STD, that is higher reaction temperatures.

At baseline, decreases could be seen in the TGA curves of the F-STD and F-BFS. The mass loss of the F-STD and F-BFS frits was 2.17 wt. % and 0.98 wt. %, respectively, according to the TGA curves. The decline in weight could be due to affinity for moisture of borosilicate glass systems, known as thirsty glasses [25].

6.3 Glass-Ceramic Coating Characterization

Figure 6.10 demonstrates the x-ray diffraction spectra of the glass-ceramics. The amorphous phase did not entirely crystallize and crystalline phases were embedded the glass matrix. The large band in the XRD patterns around 2θ: 15°-40° revealed that GC-STD and GC-BFS have amorphous network. In the SiO_2-B_2O_3-Na_2O-Al_2O_3-K_2O-F glass ceramic system, three crystal phases were detected. Ni-substituted fluorine mica ($KLiNi_2Si_4O_{10}F_2$), #PDF 00-051-0047, was the dominant crystal phase. Calcium fluoride (CaF_2) was the secondary phase, #PDF 01-087-0971. Fluorapatite ($Ca_{5.061}(P_{2.87}O_{11.46})F_{0.89}$), #PDF 01-083-0556, was a minor phase in the commercial GC-STD and eco-friendly produced GC-BFS.

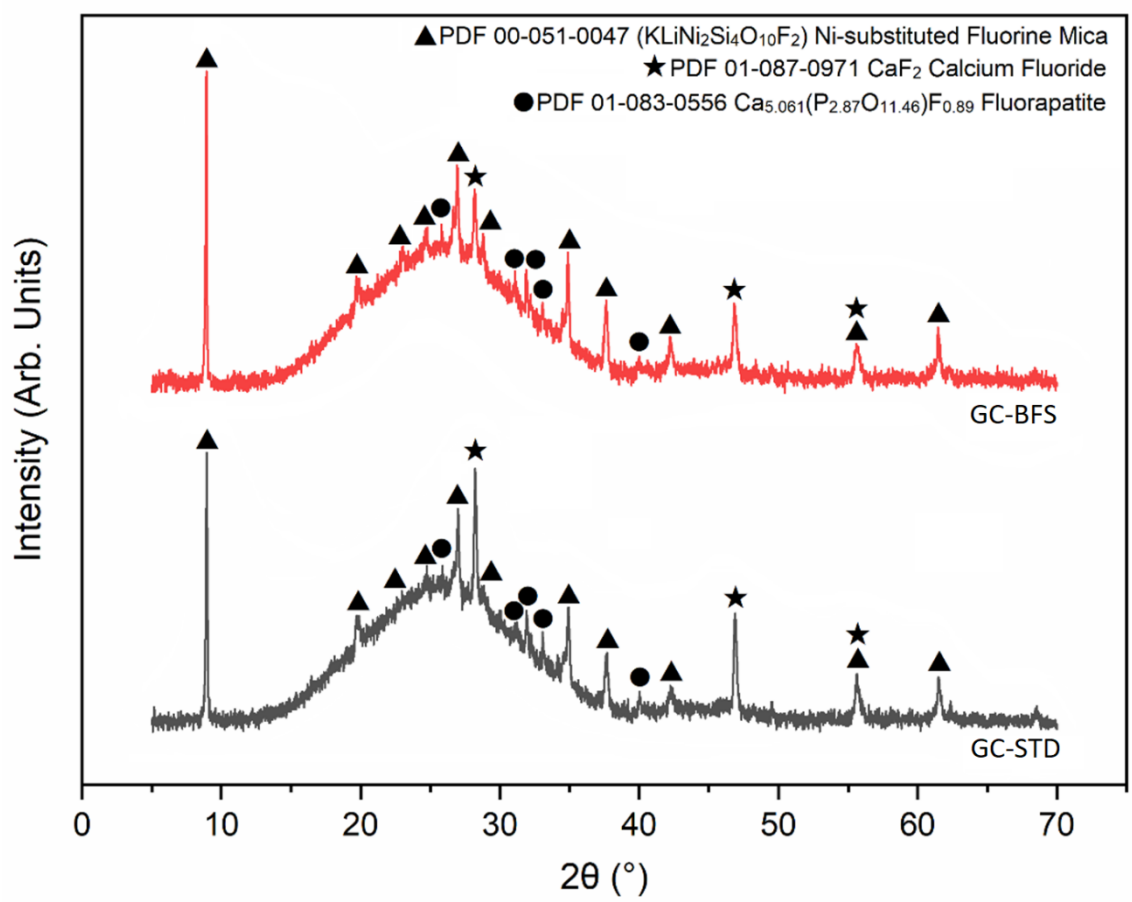

Figure 6.10 X-ray diffraction pattern of glass-ceramics

Even though both samples had the same peaks of crystalline phases, there were variations in peak intensities between GC-STD and GC-BFS.

The fluorine mica phase peak intensities of GC-BFS were greater than those of GC-STD. The increase in primary phase formation of GC-BFS could be attributed to the lower first crystallization temperature of GC-BFS compared to the GC-STD demonstrated TG-DTA analysis.

The calcium fluoride peaks from GC-STD were more intense than those from GC-BFS. Similarly, the GC-STD analysis confirmed the TG-DTA study by increasing the peak intensities of the calcium fluoride crystal phase. The complicated structure of BFS and the fluorine concentration of the frits can be responsible for differences in crystalline peak intensities between GC-STD and GC-BFS.

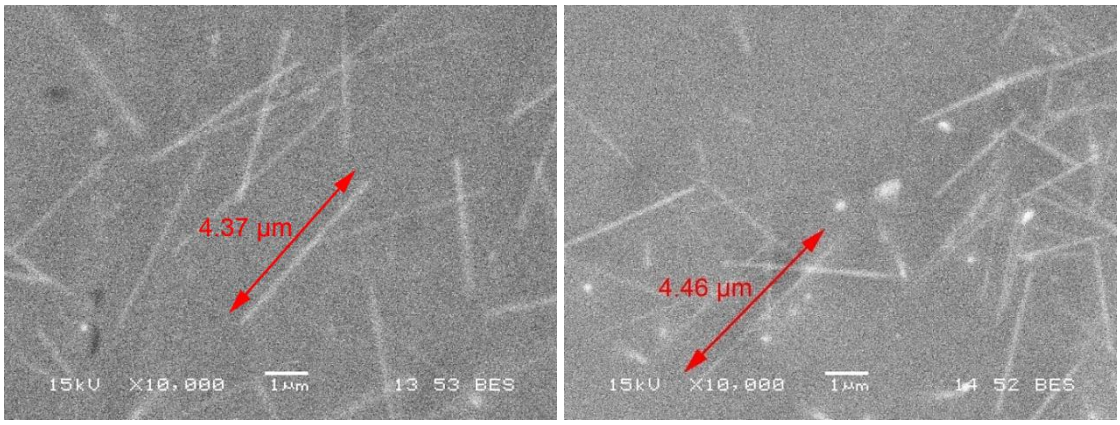

Figure 6.11 SEM images of glass-ceramic coating surfaces a) GC-STD and b) GC-BFS

The distribution and size of the phases observed by XRD were investigated using SEM examination. The SEM picture of the GC-STD acquired in BES mode is shown in Figure 6.11. (x1000 magnification). Ceramic crystals embedded in a glassy matrix were discovered using XRD and SEM images. The GC-STD and GC-BFS glass-ceramic coatings have exact surface textures. The crystals that developed resembled whiskers. For both samples, the average whisker length was found to be 4.4 ± 0.1 µm.

To understand the crystalline structure of coatings EDS analysis were addressed to the glassy matrix and whisker formed-crystalline. The SEM images and the points that EDS analysed were demonstrated in Figure 6.12 and 6.13 for GC-STD and GC-BFS, respectively. At Table 6.3 and 6.4, the chemical content of the indicated points were revealed as a result of EDS.

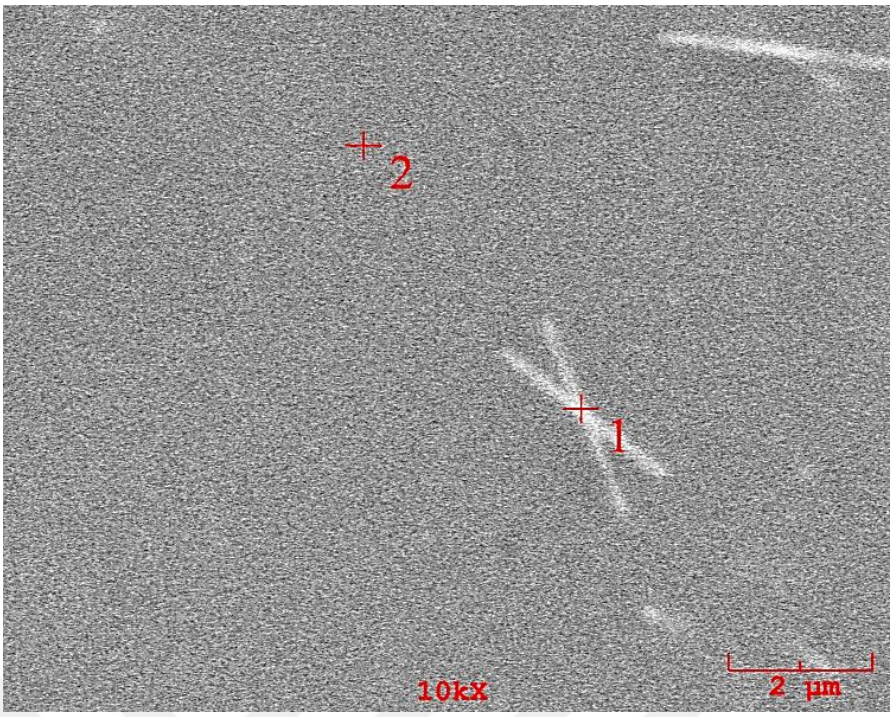

Figure 6.12 SEM-EDS images of GC-STD coating surface

Table 6.3 Chemical analysis of points and the region in GC-STD is shown in Figure 6.12. according to the EDS analysis

Elements	Point 1 %wt.	Point 2 %wt.
O	38.566	36.967
F	0.281	0.000
Na	7.607	8.616
Mg	0.797	0.755
Al	2.589	2.750
Si	31.709	36.219
P	1.038	0.000
K	2.779	2.118
Ca	5.163	2.777

Table 6.3 Chemical analysis of points and the region in GC-STD is shown in Figure 6.12. according to the EDS analysis (devamı)

Elements	Point 1 %wt.	Point 2 %wt.
Cr	0.094	0.289
Mn	0.826	0.714
Fe	1.685	0.788
Co	0.287	0.842
Ni	0.458	1.460
Cu	1.610	0.764
Zr	2.309	1.831
Mo	0.000	0.107
Ba	2.202	3.004

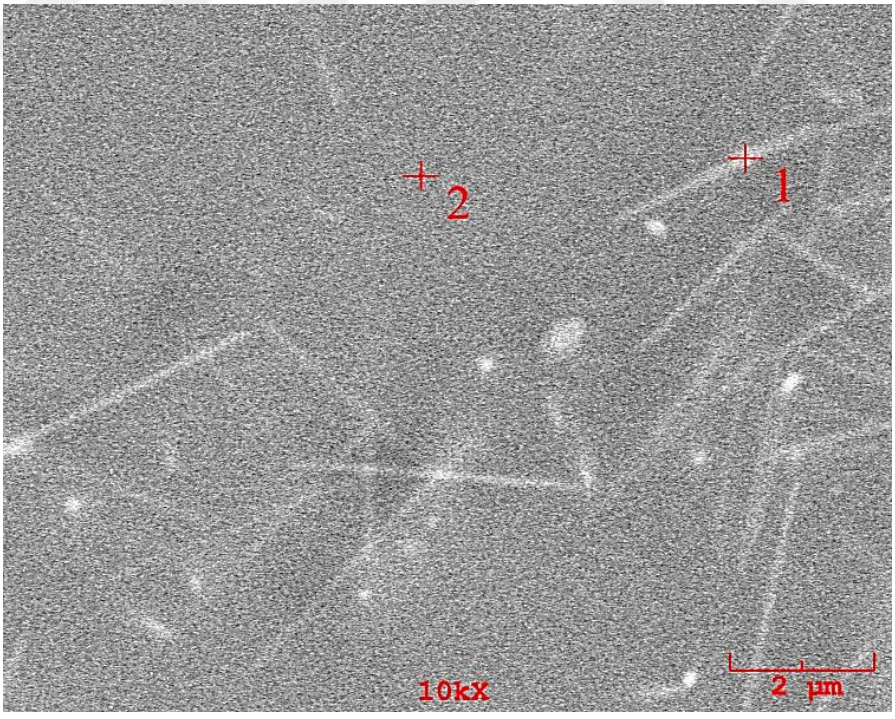

Figure 6.13 SEM-EDS images of GC-BFS coating surface

Table 6.4 Chemical analysis of points and the region in GC-BFS is shown in Figure 6.13. according to the EDS analysis

Elements	Point 1 %wt.	Point 2 %wt.
O	37.159	36.799
F	0.788	0.000
Na	7.404	8.214
Mg	0.801	1.082
Al	1.665	2.855
Si	32.137	34.543
P	0.920	0.000
K	1.909	2.160
Ca	5.332	2.054
Cr	0.403	0.415
Mn	1.117	0.584
Fe	2.448	1.808
Co	0.796	0.696
Ni	1.230	1.121
Cu	0.501	1.046
Zr	2.646	1.701
Mo	0.000	0.303
Ba	2.743	4.619

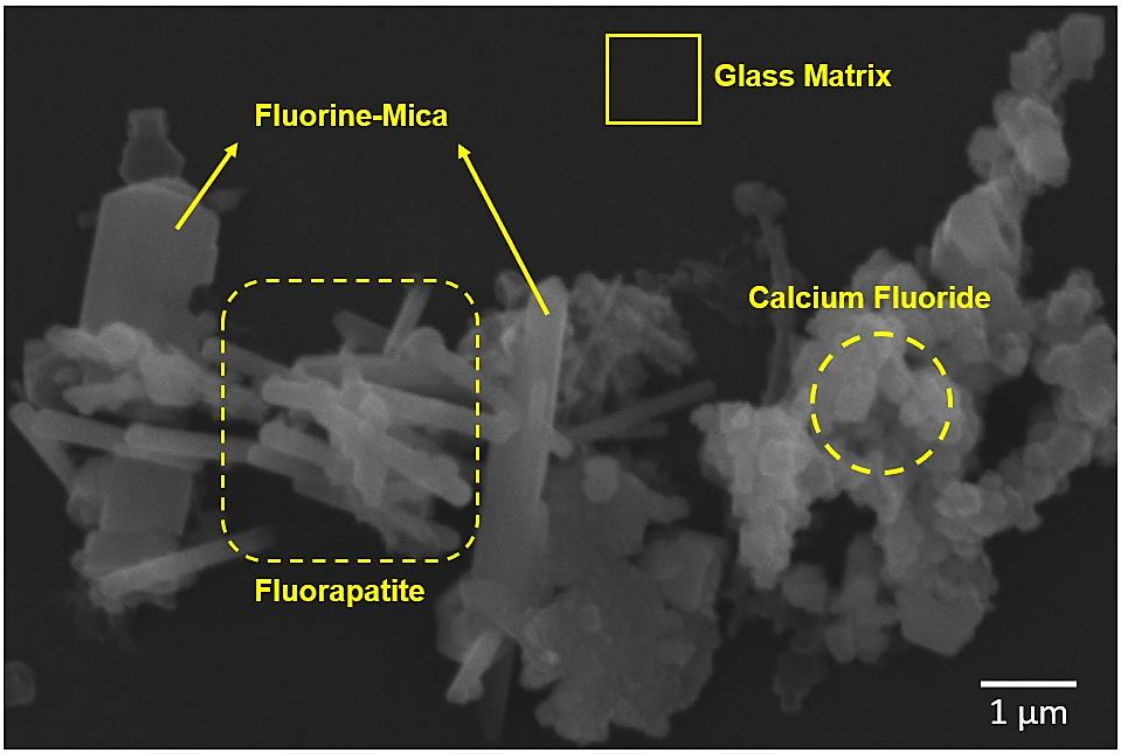

Figure 6.14 SEM imaging of crystalline structure of HF-etched glass-ceramic coatings

As a result of surface SEM analysis and EDS analysis, it was attempted to understand the crystal structure within the glass-ceramic structure. Whereas there were a requirement for further analysis to understand the crystalline structure. GC-STD and GC-BFS were chemically etched with 30% HF for 3 min for detail characterization of crystal formation in coatings and SEM analysis were employed on etched surfaces of the coatings. Thus, the glass matrix was eliminated in the glass-ceramic coating structure and the crystal structure was revealed. The most probable particle morphologies were attributed to the microstructures based on XRF, XRD, and crystal morphologies observed in the literature. The microstructures of GC-STD and GC-BFS were identical. The crystals were demonstrated on the Figure 6.14. Plate-like fluorine-mica crystals, needle-like fluorapatite crystals, and chains of calcium fluoride crystals embedded in the glass matrix were apparent in the SEM picture shown in Figure 6.14.

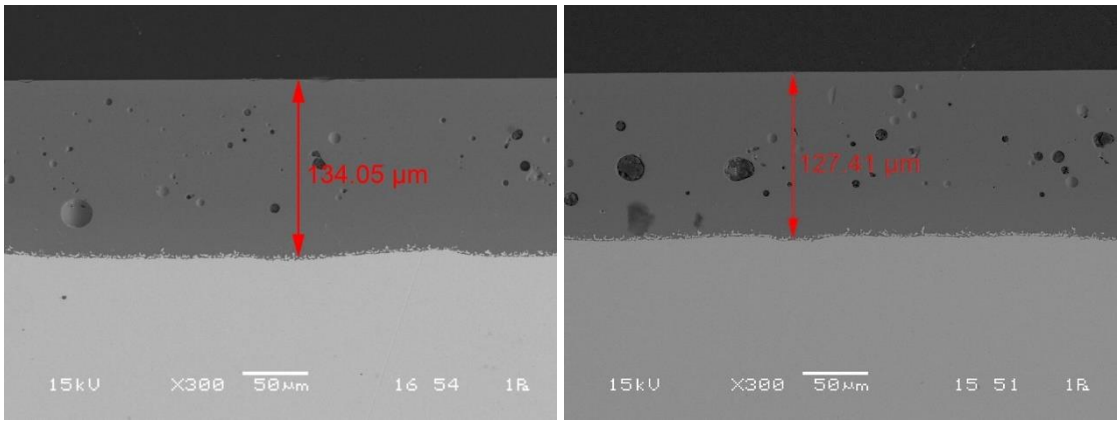

Figure 6.15 SEM imaging of cross-section between glass-ceramic coating and steel substrates a) GC-STD and b) GC-BFS

It is required that the coating adheres well to the metal and covers the surface. As the glass-ceramics coating is separated from the metal substrate with a blow or breaks after application, it makes the metal open to interaction with its environment and thus causes the corrosion process to start. In Figure 6.15, the cross-section between glass-ceramic coating and metal substrate of GC-STD and GC-BFS were demonstrated.

Adhesion mechanism can be seen, and it can be explained by four base theories: chemical, mechanical, electrolytic, and diffusion theories. The mechanical theory establishes a relationship between the coating-metal interface area, the coating metal contact area, and the adherence [26]. Metal oxide thin film layer forms on the glass-ceramic coated metal surface while it is heat-treated. However, when the temperature reaches the softening point, the coating prevents oxidation by wetting the metal surface and traps the oxide film layer between the coated metal. When the temperature increases further, the metal oxide film diffuses into the glass-ceramic coatings and creates a dendritic structure. In Figures 6.16, the anchor points are examined at the metal-glass ceramic interface were attributable to the FeCo alloy. The resulting dendritic structure provided the metal and coating to be mechanically attached to each other. However, adhesion can not be achieved mechanically alone. As the temperature rose during the firing of the coating, the iron oxide (FeO) compound consisting of the oxidized base metal plate was reduced with the NiO and CoO compounds in the frit and initiated redox reactions [26-27].

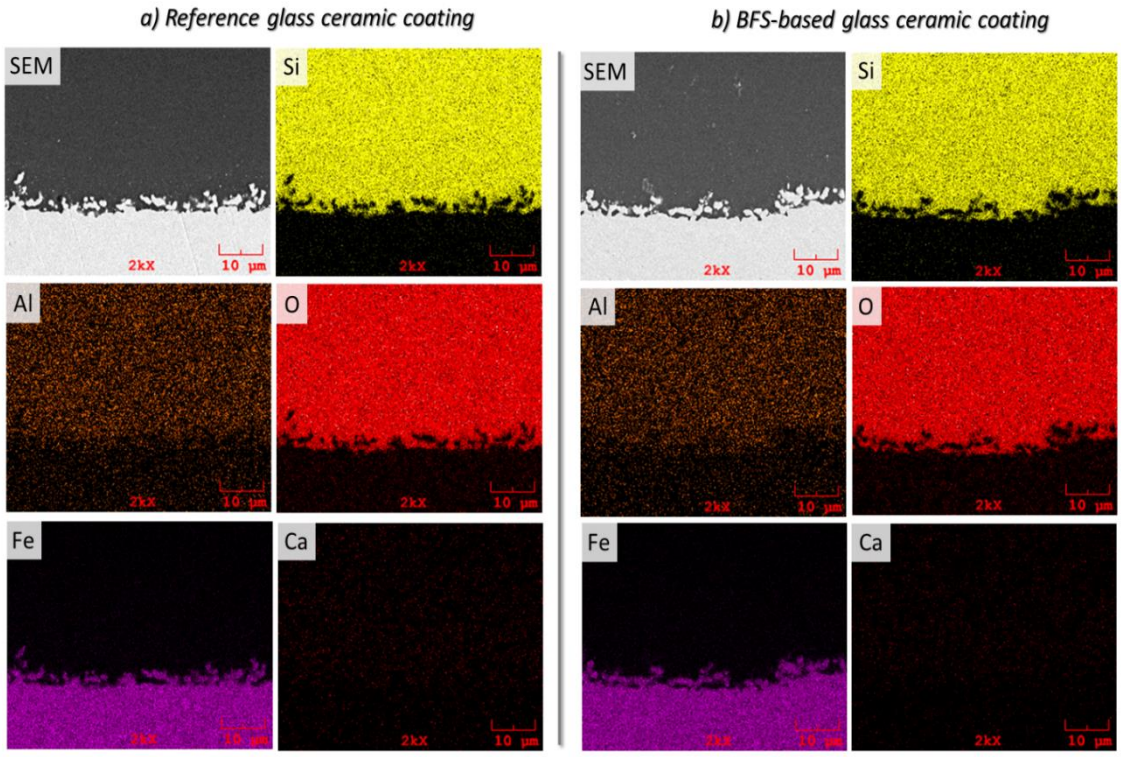

Figure 6.16 SEM-EDS Mapping images of cross-section areas of the GC-STD and GC-BFS coatings

In Figure 6.16, individual element EDS maps of Si, Al, O Fe, and Ca are presented with the given element marked on the top left corner of each map. Here, again no differences were detected between two samples in terms of interface chemical composition. Standard glass-ceramic coating content and chemical compositions were observed in the Si rich part. The ratio of iron (Fe) and cobalt (Co) is higher near the metal / glass-ceramic coating interface compared to the rest of the coating, which is consistent with the above-mentioned adhesion mechanism theories. According to the analysis results, both the reference coating and GC-BFS had strong adhesion to the steel substrate.

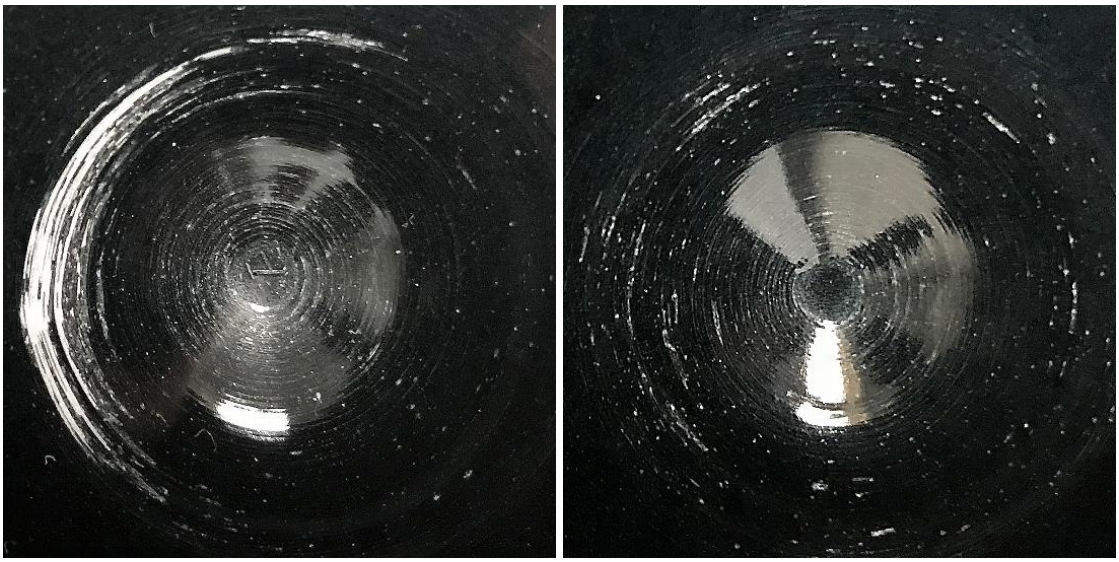

Figure 6.17 Images of Impact Test results of the coatings a) GC-STD b) GC-BFS

In addition to examining the adhesion behaviour with SEM analysis, the bonding mechanism between glass-ceramic and metal substrates was also investigated in terms of engineering properties with the impact test. The results of the impact test performed according to the BS EN ISO 10209 standard are shown in Figure 6.17. Impact test result of both GC-STD and GC-BFS were denoted as 1. As a result of the impact test, it is noticed that the adhesion of coatings were achieved optimum. It was revealed that BFS substitution to the structure does not change the impact strength.

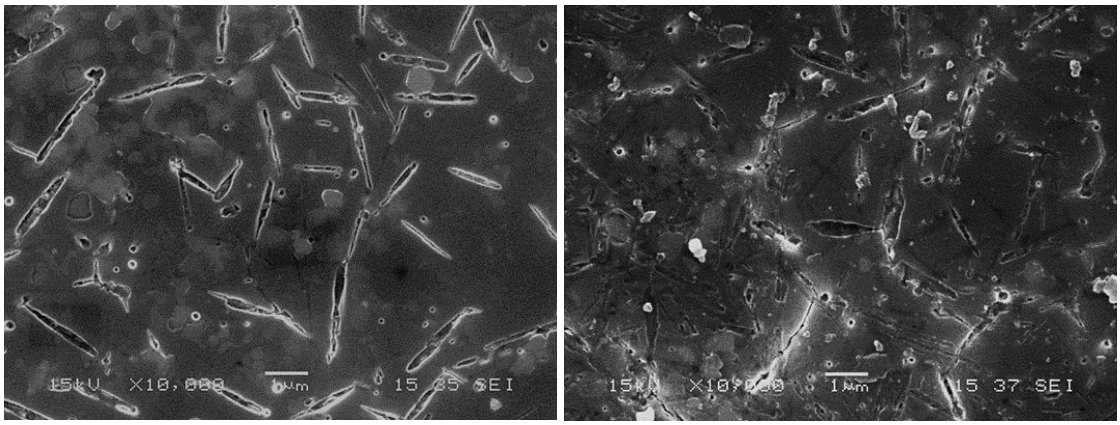

Figure 6.18 SEM images of citric acid-etched region of coatings a) GC-STD and b) GC-BFS

Glass-ceramic coated surfaces are subject to chemical corrosion depending on the application area, such as kitchenware, cookware, and oven trays. The parameter that positively affects the acid resistance is the [SiO_4] tetrahedron continuity in the

amorphous structure. In contrast, an increase in the R_2O oxides in the structure decreases the acid resistance because ions such as Li^+, Na^+, K^+ and F^- disrupts the continuity of [SiO_4] tetrahedrons and forming Si- RO structure. The solubility of the crystals and the glass phase, as well as the degree of crystallinity of the structure, are other factors that influence acid resistance [29].

With the citric acid test according to ISO 28706 on coating surfaces of GC-STD and GC-BFS, the chemical resistance behaviour of coatings were investigated. The results of the cold citric acid exposure for 15 min on surface, GC-STD and GC-BFS had similar chemical resistance which are indicated as AA. Surfaces were employed to SEM analysis after the cold citric acid exposure illustrated in Figure 6.18. The crystalline structure became much clearer in GC-STD, due to the slightly higher chemical corrosion of reference one rather than GC-BFS.

For further characterization and understanding the BFS-substitution effect on the chemical resistance of coating, GC-STD and GC-BFS were exposure boiling citric acid at 95 °C for 2.5 h. The total quantity of weight migrated from the coated surface to boiling citric acid solution were recorded using ICP-MS seen in Table 6.5.

Table 6.5 Gloss values of GC-STD and GC-BFS coatings

	Gloss Value 60˚
GC-STD	98.66 ± 3.43
GC-BFS	93.38 ± 5.96

Table 6.6 Average and standard deviations of L, a*, b* values of glass-ceramic coatings

		L	a	b
GC-STD	Average	30.118	-0.588	-1.625
	Standard Deviation	0.121	0.042	0.099
GC-BFS	Average	30.78	-0.735	-1.9275
	Standard Deviation	0.148	0.039	0.053

Gloss and colour measurements of glass ceramic coatings GC-STD and GC-BFS were investigated and shown in Table 6.6 and 6.7, respectively. Gloss values were examined in Table. According to literature, the gloss decreases with increasing SiO_2 content. Vice versa increasing the B_2O_3 content increases the gloss [120]. The evaluation of the results, i.e., the slightly high gloss value of reference glass ceramic coating (GC-STD) supports this statement. Considering the L, a*, b* values of the GC-STD and GC-BFS, it can be said that the two coatings were equivalent in terms of colour values. BFS substitution did not lead to any changes in aesthetical characteristics of GC-STD and GC-BFS.

7
CONCLUSION

BFS waste with main components of CaO, SiO_2, Al_2O_3, and MgO, as well as minor components of B_2O_3, TiO_2, Na_2O, K_2O, MnO, Fe_2O_3, BaO, and SO_3, was effectively integrated into the frit formulation as a 4% wt. replacement of commercial raw materials.

The chemical compositions of the sustainable F-BFS and F-STD with SiO_2–B_2O_3–Na_2O–Al_2O_3–K_2O–F glass-ceramic systems were identical, despite the distinct formulation for frit manufacturing in terms of raw material sources; sustainable and commercial.

F-BFS had slightly higher sintering and half-sphere temperatures than F-STD, which was ascribed to BFS's complex chemical composition, compact morphology, and refractoriness. Over the temperature range of 30–400 °C, the linear thermal expansion coefficients of the frits were determined to be 8.68 10^{-6} (1/K) for F-STD and 8.71 10^{-6} (1/K) for F-BFS. The T_G and crystallization temperatures examined in TG-DTA analysis of F-STD and F-BFS have no significant differences from each other.

The crystal structures and phase formations of frits and glass-ceramics were unaffected by BFS substitution. XRD and SEM examination indicated that the predominant crystal phase of GC-STD and GC-BFS was Ni-substituted fluorine mica ($KLiNi_2Si_4O_{10}F_2$). Other crystalline phases were also exact: Fluorapatite ($Ca_{5.061}(P_{2.87}O_{11.46})F_{0.89}$) and Calcium fluoride ($CaF_2$).

The higher T_G examined in TG-DTA and hence higher amorphous structure investigated by XRD of GC-BFS resulted in a stronger acid resistance than the GC-STD.

The chemistry of GC-BFS did not affect negatively from using of BFS and the engineering properties of partially sustainable produced GC-BFS final coatings had similar characteristics with commercially produced GC-STD coating.

This work establishes proof-of-concept, which is required for BFS waste to be used in large-scale manufacturing without pre-treatment. The sustainable production approach

for glass-ceramic coatings was successfully achieved by utilizing BFS as sustainable quartz (SiO_2), calcium carbonate ($CaCO_3$), alumina (Al_2O_3) etc. raw material sources.

REFERENCES

[1] I. Yuksel, “Blast-furnace slag,” in *Waste and Supplementary Cementitious Materials in Concrete: Characterisation, Properties and Applications*, Elsevier, 2018, pp. 361–415. doi: 10.1016/B978-0-08-102156-9.00012-2.

[2] M. Reuter, Y. Xiao, and U. Boin, “Recycling and environmental issues of metallurgical slags and salt fluxes,” in *VII International Conference on MoltenSlags Fluxes and Salts,The South African Institute of Mining and Metallurgy*, 2004, pp. 349–356.

[3] M. Tokyay, *Cement and Concrete Mineral Admixtures*. New York: CRC Press, 2016.

[4] *Mineral Commodity Summaries*, vol. 01. U.S. Geological Survey, 2020.

[5] P. G. S. A. JeyaSundar, A. Ali, D. Guo, and Z. Zhang, “Waste treatment approaches for environmental sustainability,” in *Microorganisms for Sustainable Environment and Health*, Elsevier, 2020, pp. 119–135. doi: 10.1016/B978-0-12-819001-2.00006-1.

[6] Z. Bayer Ozturk and E. Eren Gultekin, “Preparation of ceramic wall tiling derived from blast furnace slag,” *Ceramics International*, vol. 41, no. 9, pp. 12020–12026, Nov. 2015, doi: 10.1016/j.ceramint.2015.06.014.

[7] E. Karamanova, G. Avdeev, and A. Karamanov, “Ceramics from blast furnace slag, kaolin and quartz,” *J Eur Ceram Soc*, vol. 31, no. 6, pp. 989–998, Jun. 2011, doi: 10.1016/j.jeurceramsoc.2011.01.006.

[8] I. Ozdemir and S. Yilmaz, “Processing of unglazed ceramic tiles from blast furnace slag,” *Journal of Materials Processing Technology*, vol. 183, no. 1, pp. 13–17, Mar. 2007, doi: 10.1016/j.jmatprotec.2006.09.002.

[9] Y. Zhao, D. Chen, Y. Bi, and M. Long, “Preparation of low cost glass-ceramics from molten blast furnace slag,” *Ceramics International*, vol. 38, no. 3, pp. 2495–2500, Apr. 2012, doi: 10.1016/j.ceramint.2011.11.018.

[10] A. A. Francis, “Conversion of blast furnace slag into new glass-ceramic material,” *J Eur Ceram Soc*, vol. 24, no. 9, pp. 2819–2824, Aug. 2004, doi: 10.1016/j.jeurceramsoc.2003.08.019.

[11] J. Ma *et al.*, “Crystallization of CaO–MgO–Al2O3–SiO2 glass ceramic derived from blast furnace slag via one-step method,” *Materials Chemistry and Physics*, vol. 261, Mar. 2021, doi: 10.1016/j.matchemphys.2020.124213.

[12] R. Baldusco, T. R. S. Nobre, S. C. Angulo, V. A. Quarcioni, and M. A. Cincotto, “Dehydration and Rehydration of Blast Furnace Slag Cement,” *Journal of Materials in Civil Engineering*, vol. 31, no. 8, p. 04019132, Aug. 2019, doi: 10.1061/(asce)mt.1943-5533.0002725.

[13] Z. Bencze and L. Gaspar, “Blast Furnace Slag In Road Construction and Maintenance,” *Dorogi i Mosti 2021*, pp. 53–59, 2021.

[14] E. Sakai, T. Ansai, D. Atarashi, and Y. Ikeo, “Material design of high-volume blast furnace slag cement in consideration of early hydration of cement,” *Cem. Sci. Concr. Technol.*, vol. 65, pp. 20–26, 2011.

[15] A. I. Andrews, S. Pagliuca, and W. D. Faust, *Porcelain (Vitreous) Enamels - Industrial Enamelling Processes*. Mantova: International Enamellers Institue, 2011.

[16] R. A. Eppler and D. Eppler, *Glazes and glass coatings*. Ohio: The American Ceramic Society, 2000.

[17] W. Holland and G. Beall, *in: Glass-Ceramic Technology*. Westerville, OH: The American Ceramic Society, 2002.

[18] J. Deubener *et al.*, “Updated definition of glass-ceramics,” *Journal of Non-Crystalline Solids*, vol. 501, pp. 3–10, Dec. 2018, doi: 10.1016/j.jnoncrysol.2018.01.033.

[19] A. R. Allu *et al.*, “Understanding the formation of CaAl2Si2O8 in melilite-based glass-ceramics: Combined diffraction and spectroscopic studies,” *ACS Omega*, vol. 2, no. 9, pp. 6233–6243, Sep. 2017, doi: 10.1021/acsomega.7b00598.

[20] W. A. Deer, R. A. Howie, and J. Zussman, *An Introduction to Rock-Forming Minerals*. London: The Mineralogical Society, 2013.

[21] C. Venturelli, “Heating Microscopy and its Applications,” *Microscopy Today*, vol. 19, no. 1, pp. 20–25, Jan. 2011, doi: 10.1017/s1551929510001185.

[22] A. I. Andrews, S. Pagliuca, and W. D. Faust, *Metallic substrate for enamelling, in: Porcelain (Vitreous) Enamels and Industrial Enamelling Processes the Preparation, Application and Properties of Enamels*. Mantova: Tipografia Commerciale, 2011.

[23] S. Wu, Q. Zhou, Y. J. Wang, M. Zhang, and Y. J. Chen, “Effect of fluorine content on the crystallization and flexural strength of fluoro-mica glass ceramics,” *Ceramics International*, vol. 39, no. 4, pp. 4187–4190, May 2013, doi: 10.1016/j.ceramint.2012.10.275.

[24] K. Cheng, J. Wan, and K. Liang, “Effect of fluorine source on crystallization of R 2 O-MgO-Al2O3-B2O3-SiO2-F(R=K+,Na+) glasses,” 1999. [Online]. Available: www.elsevier.com/locate/msea

[25] A. Rafferty, R. G. Hill, and D. Wood, “An investigation into the amorphous phase separation characteristics of an ionomer glass series and a sodium-boro-silicate glass system,” pp. 2311–2319, 2003.

[26] A. H. Dietzel, *Emaillierung: Wissenschaftliche Grundlagen und Grundzüge der Technologie, Scientific principles and fundamentals of technology*. Berlin: Springer, 1981.

[27] B. W. King, H. P. Tripp, and W. H. Duckworth, “Nature of Adherence of Porcelain Enamels to Metals,” 1959.

[28] A. Petzold and H. Pöschmann, *Email und Emailliertechnik: Ein Lehrbuch in 3 Teilen*. VEB Deutscher Verlag fuer Grundstoffindustrie, 1986.

[29] G. S. Frankel *et al.*, “A comparative review of the aqueous corrosion of glasses, crystalline ceramics, and metals,” *npj Materials Degradation*, vol. 2, no. 1. Nature, Dec. 01, 2018. doi: 10.1038/s41529-018-0037-2.

[30] W. Deng, J. S. Cheng, P. J. Tian, and M. T. Wang, “Chemical durability and weathering resistance of canasite based glass and glass-ceramics,” *Journal of Non-Crystalline Solids*, vol. 358, no. 21, pp. 2847–2854, Oct. 2012, doi: 10.1016/j.jnoncrysol.2012.07.003.

[31] N. Salman Hassan, “Studying The Effect of Zircon Dioxide on The Corrosion Resistance of Porcelain Enamel,” 2011.

[32] S. Rossi, M. Fedel, F. Deflorian, and N. Parziani, “Abrasion and chemical resistance of composite vitreous enamel coatings with hard particles,” in *Surface and Interface Analysis*, Aug. 2016, vol. 48, no. 8, pp. 827–837. doi: 10.1002/sia.5849.

[33] S. D. Stookey, “History of the Development of Pyroceram,” *Research Management*, vol. 1, no. 3, pp. 155–163, Sep. 1958, doi: 10.1080/00345334.1958.11755484.

[34] F. A. Hummel, “Thermal Expansion Properties of Some Synthetic Lithia Minerals,” 1951.

[35] W. Holland and G. H. Beall, *Glass-Ceramic Technology*, 3rd Edition., vol. 3rd Edition. New Jersey: Wiley - American Ceramic Society, 2020.

[36] S. Rossi, F. Deflorian, L. Fontanari, A. Cambruzzi, and P. L. Bonora, “Electrochemical measurements to evaluate the damage due to abrasion on organic protective system,” in *Progress in Organic Coatings*, Apr. 2005, vol. 52, no. 4, pp. 288–297. doi: 10.1016/j.porgcoat.2004.09.005.

[37] V. Günay and Ş. Yılmaz, *Glass Ceramics: Science and Technology (Cam Seramikler: Bilim ve Teknolojisi)*. Kocaeli: Tübitak Marmara Araştırma Merkezi, 2010.

[38] P. W. McMillan, *Crystallization of a Glass-Ceramic by Epitaxial Growth*. London: Academic Press, 1979.

[39] Headley T. J. and Loehman R. E., “Crystallization of a Glass-Ceramic by Epitaxial Growth,” *Journal of the American Ceramic Society*, pp. 620–625, 1983.

[40] J. Shi and X. Feng, “Laser-induced nonlinear crystalline waveguide on glass fiber format and diode-pumped second harmonic generation,” *Optical Fiber Technology*, vol. 41, pp. 118–124, Mar. 2018, doi: 10.1016/j.yofte.2018.01.015.

[41] S. Fujita and S. Tanabe, “Fabrication, microstructure and optical properties of Er3+:YAG glass-ceramics,” *Opt Mater (Amst)*, vol. 32, no. 9, pp. 886–890, 2010, doi: 10.1016/j.optmat.2010.01.014.

[42] M. Kamnoy, U. Intatha, A. Munpakdee, S. Eitssayeam, and T. Tunkasiri, “Mechanical properties and microstructure of Li2O-SiO2-P2O5-Al2O3-K2O-CaO glass-ceramics,” in *Key Engineering Materials*, 2018, vol. 766 KEM, pp. 164–169. doi: 10.4028/www.scientific.net/KEM.766.164.

[43] C. Lee, I. S. Kim, and B. Lee, “Slow crack growth in a cordierite-based glass–ceramic missile radome due to stress corrosion,” *Engineering Failure Analysis*, vol. 93, pp. 76–86, Nov. 2018, doi: 10.1016/j.engfailanal.2018.04.007.

[44] G. H. Beall, “Design and Properties Of Glass-Ceramics,” *Annu. Rev. Mater. Sci*, vol. 22, no. 1, pp. 91–119, Aug. 1992, doi: 10.1146/annurev.ms.22.080192.000515.

[45] H. S. Maiti, “Transparent and Machinable Glass-Ceramics,” in *Handbook of Advanced Ceramics and Composites*, Springer International Publishing, 2020, pp. 461–493. doi: 10.1007/978-3-030-16347-1_13.

[46] W. Ostertag, G. R. Fischer, and J. P. Williams, “Thermal Expansion of Synthetic **β**-Spodumene and **β**-Spodumene-Silica Solid Solutions,” *J. Am. Ceram. Soc.*, vol. 51, no. 11, pp. 651–654, 1968, doi: 10.1111/j.1151- 2916.1968.tb12638.x.

[47] L. Kang, T. Liu, Z. Su, and Y. Kong, “Research on glass ceramics with negative coefficient of thermal expansion used as fiber Bragg grating substrate,” in *Materials, Active Devices, and Optical Amplifiers*, May 2004, vol. 5280, p. 638. doi: 10.1117/12.520427.

[48] E. El-Meliegy and R. van Noort, *Glasses and glass ceramics for medical applications*, vol. 9781461412281. Springer New York, 2012. doi: 10.1007/978-1-4614-1228-1.

[49] A. Herczog, “Application of Glass-Ceramics for Electronic Components and Circuits,” *IEEE Trans. Parts, Hybrids, Packag*, vol. 9, no. 4, pp. 247–255, 1973, doi: 10.1109/TPHP.1973.1136735.

[50] A. Sakamoto and S. Yamamoto, “Glass-Ceramics: Engineering Principles and Applications,” *International Journal of Applied Glass Science*, vol. 1, no. 3, pp. 237–247, Sep. 2010, doi: 10.1111/j.2041-1294.2010.00027.x.

[51] H. Wang, J. Liu, J. Zhai, and B. Shen, “Ultra High Energy-Storage Density in the Barium Potassium Niobate-Based Glass-Ceramics for Energy-Storage

Applications," *Journal of the American Ceramic Society*, vol. 99, no. 9, pp. 2909–2912, 2016, doi: 10.1111/jace.14446.

[52] X. Fu, C. H. Zhang, C. Q. Li, K. J. Li, and Y. B. Zuo, "Design and processing of temperature resistant enamel coating materials," in *Applied Mechanics and Materials*, 2014, vol. 457–458, pp. 168–171. doi: 10.4028/www.scientific.net/AMM.457-458.168.

[53] L. Samiee, H. Sarpoolaky, and A. Mirhabibi, "Microstructure and adherence of cobalt containing and cobalt free enamels to low carbon steel," *Materials Science and Engineering A*, vol. 458, no. 1–2, pp. 88–95, Jun. 2007, doi: 10.1016/j.msea.2006.12.108.

[54] E. Yılmaz, "Taban Malzemeye Emaye Arayüz İlişkilerinin Emaye Kalitesine Etkisi," Yüksek Lisans Tezi, İstanbul Teknik Üniversitesi Fen Bilimleri Enstitüsü, İstanbul, 2014.

[55] I. A. Shimanskiy, V. G. Babkin, V. K. Frizorger, E. S. Goloskin, and A. B. Nabiulin, "Influence of Initial Components Mechanical Activation on the Properties of Protective Enamel Coating on the Cast-Iron Surface," 2012.

[56] F. Russo, S. Rossi, and A. M. Compagnoni, "Porcelain Enamel Coatings," *Encyclopedia*, vol. 1, no. 2, pp. 388–400, Apr. 2021, doi: 10.3390/encyclopedia1020032.

[57] E. Güngör, "Termik Santrallerin Döner Tip Hava Isıtıcılarında Kullanılan Isı Değiştirici Plakalar İçin Emaye Kaplama Optimizasyonu," Yüksek Lisans Tezi, İstanbul Teknik Üniversitesi Fen Bilimleri Enstitüsü, İstanbul, 2015.

[58] B. Karasu, İ. Saçkan, and M. C. Tapli, "Enamel from past to present time," *El-Cezeri Journal of Science and Engineering*, vol. 7, no. 2, pp. 923–939, 2020, doi: 10.31202/ecjse.660254.

[59] "Vitreous Enamel Association, 'VEA,' Media & Marketing Services and CWN Design," Feb. 15, 2020. https://www.vea.org.uk/what-is-enamel/ (accessed Feb. 15, 2020).

[60] "The Vitreous Enameller's Association, 'The Institute of Materials, Minerals and Mining,' HM The Queen," 2020. https://www.iom3.org/vitreous-enamellers-society/concise-history- enamel (accessed Feb. 15, 2020).

[61] “ISO, ‘International Organization for Standardization,’” 2020. https://www.iso.org/ics/25.220.50/x/ (accessed May 16, 2020).

[62] “The Porcelain Enamel Institute, Inc., ‘PEI,’ AOL,” 2020. http://porcelainenamel.com/501_-_Appearance/ (accessed Feb. 15, 2020).

[63] “The International Enamellers Institute, ‘IEI,’ 1 lova,” 2020. http://www.iei-world.org/pagine/enamel.asp (accessed Feb. 15, 2020).

[64] W. D. Faust, “Porcelain (Vitreous) Enamels and Industrial Enamelling Processes,” Ohio, 2012.

[65] A. A. Andrews, S. Pagliuce, and W. D. Faust, *“Raw Materials for Enamels,” in Porcelain Enamels: The Preparation, Application and Properties of Enamels*. Mantova: Tipografia Commerciale, 2011.

[66] K. Benzesik, M. İ. Terzioğlu, F. Sahin, and O. Yucel, “Optimizing the Migration Behavior of Enamel Coatings Used as Food Contact Materials,” Oct. 2018. [Online]. Available: https://www.researchgate.net/publication/329327438

[67] A. P. Tomsia and A. Pask, “Chemical reactions and adherence at glass/metal interfaces: an analysis,” 1986.

[68] A. I. Andrews, S. Pagliuca, and W. D. Faust, *Enamel Properties and Tests, Porcelain (Vitreous) Enamels and Industrial Enamelling Processes The Preparation, Application and Properties of Enamels*. Mantova: Tipografia Commerciale, 2011.

[69] A. I. Andrews, S. Pagliuca, and W. D. Faust, *Fudamentals and Cosiderations, Porcelain (Vitreous) Enamels and Industrial Enamelling Processes The Preparation, Application and Properties of Enamels*. Mantova: Tipografia Commerciale, 2011.

[70] ASTM C385-58, “Standard Test Method for Thermal Shock Resistance of Porcelain-Enameled Utensils,” Pennsylvania, 2018.

[71] M. Garcia-Valles *et al.*, “Calculation of viscosity-temperature curves for glass obtained from four wastewater treatment plants in Egypt,” *Journal of Thermal Analysis and Calorimetry*, vol. 111, no. 1, pp. 107–114, Jan. 2013, doi: 10.1007/s10973-012-2232-7.

[72] M. Shu, H. Yin, Q. Zhong, X. Shi, and H. Han, “Effect of glass powder on acid resistance of enamel coating,” *Surface Review and Letters*, vol. 24, no. 3, Apr. 2017, doi: 10.1142/S0218625X17500366.

[73] A. I. Andrews, S. Pagliuca, and W. D. Faust, *“Chemical and Electrical Properties,” in Porcelain (Vitreous) Enamels and Industrial Enamelling Processes The Preparation, Application and Properties of Enamels*. Mantova: Tipografia Commerciale, 2011.

[74] E. Scrinzi and S. Rossi, “The aesthetic and functional properties of enamel coatings on steel,” *Materials and Design*, vol. 31, no. 9, pp. 4138–4146, Oct. 2010, doi: 10.1016/j.matdes.2010.04.030.

[75] S. Baycık, “Granüle Yüksek Fırın Cüruflarının Karo Sektöründe Kullanılabilirliğinin Araştırılması,” Yüksek Lisans Tezi, İstanbul Technical University, İstanbul, 2003.

[76] Arcelor Mittal, “Steel for enamelling and enamelled steel.”

[77] A. Davran, “Enamelling Applications On Metal From Past to Future,” MASTER THESİS, IZMIR UNIVERSITY, İzmir, 2011.

[78] L. Besra and M. Liu, “A review on fundamentals and applications of electrophoretic deposition (EPD),” *Progress in Materials Science*, vol. 52, no. 1. pp. 1–61, Jan. 2007. doi: 10.1016/j.pmatsci.2006.07.001.

[79] P. Amrollahi, J. S. Krasinski, R. Vaidyanathan, L. Tayebi, and D. Vashaee, “Electrophoretic Deposition (EPD): Fundamentals and Applications from Nano- to Micro-Scale Structures,” in *Handbook of Nanoelectrochemistry*, Springer International Publishing, 2015, pp. 1–27. doi: 10.1007/978-3-319-15207-3_7-1.

[80] M. R. Dorfman, “Thermal spray coatings,” in *Handbook of Environmental Degradation Of Materials: Third Edition*, Elsevier Inc., 2018, pp. 469–488. doi: 10.1016/B978-0-323-52472-8.00023-X.

[81] P. Fauchais and A. Vardelle, “Thermal Sprayed Coatings Used Against Corrosion and Corrosive Wear,” *Advanced Plasma Spray Applications, InTech*, 2012, doi: 10.5772/34448.

[82] T. Zhang, Y. Bao, and D. T. Gawne, “Process model of plasma enamelling,” pp. 1019–1026, 2003, [Online]. Available: www.elsevier.com/locate/jeurceramsoc

[83] D. Thomas, “Ceramic Engineering and Science Proceedings,” *Proceedings of the 59th Porcelain Enamel Institute Technical forum*, vol. 18, no. 5, 1997.

[84] “Metallurgical Industry Automation,” *EPA*, vol. 86, no. 1, 2011.

[85] P. C. Chiang and S. Y. Pan, *Carbon dioxide mineralization and utilization*. Springer, 2017. doi: 10.1007/978-981-10-3268-4.

[86] G. C. Wang, “Ferrous metal production and ferrous slags,” in *The Utilization of Slag in Civil Infrastructure Construction*, Elsevier, 2016, pp. 9–33. doi: 10.1016/b978-0-08-100381-7.00002-1.

[87] K. Horii, T. Kato, K. Sugahara, N. Tsutsumi, and Y. Kitano, “Overview of IronSteel Slag Application and Development of New Utilization Technologies,” pp. 5–11, 2015.

[88] J. O’Connor *et al.*, “Production, characterisation, utilisation, and beneficial soil application of steel slag: A review,” *Journal of Hazardous Materials*, vol. 419, Oct. 2021, doi: 10.1016/j.jhazmat.2021.126478.

[89] K. Horii, N. TSUTSUMI, T. KATO, Y. KITANO, and K. SUGAHARA, “Overview of iron/steel slag application and development of new utilization technologies,” *Nippon Steel & Sumitomo Metal Technical Report*, vol. 109, no. 109, pp. 5–11, 2015.

[90] I. H. Aziz *et al.*, “Recent Developments in Steelmaking Industry and Potential Alkali Activated Based Steel Waste : A Comprehensive Review,” 2022.

[91] L. Wang and F. Aslani, “Electrical resistivity and piezoresistivity of cement mortar containing ground granulated blast furnace slag,” *Construction and Building Materials*, vol. 263, p. 120243, 2020, doi: 10.1016/j.conbuildmat.2020.120243.

[92] J. L. Vilaplana, F. J. Baeza, O. Galao, E. G. Alcocel, E. Zornoza, and P. Garcés, “Mechanical properties of alkali activated blast furnace slag pastes reinforced with carbon fibers,” *Construction and Building Materials*, vol. 116, pp. 63–71, 2016, doi: 10.1016/j.conbuildmat.2016.04.066.

[93] W. Pacierpnik, W. Nocuń-Wczelik, and E. Kapeluszna, “Application of weathered granulated blast furnace slag as a supplementary cementitious material

in concrete," *Archives of Civil Engineering*, vol. 66, no. 4, pp. 381–398, 2020, doi: 10.24425/ace.2020.135227.

[94] R. Martinez-Lopez and J. Ivan Escalante-Garcia, "Alkali activated composite binders of waste silica soda lime glass and blast furnace slag: Strength as a function of the composition," *Construction and Building Materials*, vol. 119, pp. 119–129, 2016, doi: 10.1016/j.conbuildmat.2016.05.064.

[95] K. C. Curry, "Slag - Iron and Steel," 2021. [Online]. Available: https://www.trademining.com/index.jsp.

[96] Y. Liu, Y. Su, G. Xu, Y. Chen, and G. You, "Research Progress on Controlled Low-Strength Materials: Metallurgical Waste Slag as Cementitious Materials," *Materials*, vol. 15, no. 3. MDPI, Feb. 01, 2022. doi: 10.3390/ma15030727.

[97] I. H. Aziz *et al.*, "Recent Developments in Steelmaking Industry and Potential Alkali Activated Based Steel Waste: A Comprehensive Review," *Materials*, vol. 15, no. 5. MDPI, Mar. 01, 2022. doi: 10.3390/ma15051948.

[98] B. Das, S. Prakash, P. S. R. Reddy, and V. N. Misra, "An overview of utilization of slag and sludge from steel industries," *Resources, Conservation and Recycling*, vol. 50, no. 1, pp. 40–57, Mar. 2007, doi: 10.1016/j.resconrec.2006.05.008.

[99] L. Wang and F. Aslani, "Electrical resistivity and piezoresistivity of cement mortar containing ground granulated blast furnace slag," *Construction and Building Materials*, vol. 263, Dec. 2020, doi: 10.1016/j.conbuildmat.2020.120243.

[100] M. C. S. U.S. Geological Survey, "Iron and Steel Slag," *U.S. Geol. Surv. Miner. Commod. Summ.*, no. 703, pp. 1–2, 2022.

[101] worldsteel, "Life cycle inventory (LCI) study 2020 data release Seventh global LCI study for steel products 2020 LCI Study Report," 2020.

[102] T. E. S. A. Eurofer, "European Steel in Figures 2021," 2020.

[103] G. C. Wang, "Slag processing," in *The Utilization of Slag in Civil Infrastructure Construction*, Elsevier, 2016, pp. 87–113. doi: 10.1016/b978-0-08-100381-7.00005-7.

[104] Sasaki T, “Standardization of Iron and Steel Slag Products,” pp. 189–194, 2015.

[105] Y. Fan, F. He, Z. Li, Z. Li, W. Zhang, and J. Xie, “Sintering Mechanism, Structure and Crystallisation of CaO-MgO-Al2O3-SiO2 Glass-Ceramics From Blast Furnace Slag,” *Ceramics - Silikaty*, vol. 65, no. 4, pp. 334–343, 2021, doi: 10.13168/cs.2021.0035.

[106] H.-X. Lu *et al.*, “A preparation and performance study of glass-ceramic glazes derived from blast furnace slag and fly ash,” *Journal of Ceramic Processing Research*, vol. 12, no. 5, pp. 588–591, 2011.

[107] L. Ding, W. Ning, Q. Wang, D. Shi, and L. Luo, “Preparation and characterization of glass-ceramic foams from blast furnace slag and waste glass,” *Materials Letters*, vol. 141, pp. 327–329, Feb. 2015, doi: 10.1016/j.matlet.2014.11.122.

[108] T. Sofilić, U. Sofilić, and I. Brnardić, “The Significance of Iron And Steel Slag As By-Product For Utilization In Road Construction,” 2012, pp. 421–436. [Online]. Available: www.simet.hr/~foundry

[109] H. R. Quintana, S. Chaves-Pabón, and D. A. Escobar, “Evaluation of a Warm Mix Asphalt Manufactured with Blast Furnace Slag,” *Modern Applied Science*, vol. 12, no. 12, p. 28, Nov. 2018, doi: 10.5539/mas.v12n12p28.

[110] Speight J. G., “Asphalt Materials Science and Technology,” 2015, p. 921.

[111] J. D. Ríos, A. Vahí, C. Leiva, A. M. Martínez-De la Concha, and H. Cifuentes, “Analysis of the utilization of air-cooled blast furnace slag as industrial waste aggregates in self-compacting concrete,” *Sustainability (Switzerland)*, vol. 11, no. 6, 2019, doi: 10.3390/su11061702.

[112] A. Qi, X. Liu, Z. Wang, and Z. Chen, “Mechanical properties of the concrete containing ferronickel slag and blast furnace slag powder,” *Construction and Building Materials*, vol. 231, Jan. 2020, doi: 10.1016/j.conbuildmat.2019.117120.

[113] G. C. Ulubeyli and R. Artir, “Sustainability for Blast Furnace Slag: Use of Some Construction Wastes,” *Procedia - Social and Behavioral Sciences*, vol. 195, pp. 2191–2198, Jul. 2015, doi: 10.1016/j.sbspro.2015.06.297.

[114] D. C. Sekhar and S. Nayak, “Utilization of granulated blast furnace slag and cement in the manufacture of compressed stabilized earth blocks,” *Construction and Building Materials*, vol. 166, pp. 531–536, Mar. 2018, doi: 10.1016/j.conbuildmat.2018.01.125.

[115] S. Park, “Simulating the carbonation of calcium sulfoaluminate cement blended with supplementary cementitious materials,” *Journal of CO2 Utilization*, vol. 41, Oct. 2020, doi: 10.1016/j.jcou.2020.101286.

[116] X. Liu, Y. Li, L. Zhang, and D. Cang, “Utilization of CFB fly ash in Eco-cement: Mechanical properties and microstructural analysis,” in *Advanced Materials Research*, 2011, vol. 150–151, pp. 885–889. doi: 10.4028/www.scientific.net/AMR.150-151.885.

[117] T. Kanda, H. Momose, K. Ishizeki, K. I. Imamoto, and C. Kiyohara, “Impacts of trace additives and early-stage curing conditions on the shrinkage cracking resistance of blast-furnace slag cement concrete,” *Journal of Advanced Concrete Technology*, vol. 14, no. 8, pp. 475–488, 2016, doi: 10.3151/jact.14.475.

[118] O. Rubem *et al.*, “Sintering Behavior of LZSA Glass-Ceramics,” 2009.

[119] P. G. Debenedetti and F. H. Stillinger, “Supercooled liquids and the glass transition,” 2001. [Online]. Available: www.nature.com

[120] Bianca, “Emaillierungen für Edelstähle,” 2007.

PUBLICATIONS FROM THE THESIS

SCI Papers

1. Ceramics International

"Development of CaO-rich Blast Furnace Slag Containing Fluorine Mica-based Glass-Ceramic Coatings"

Volume 47, Issue 21, 2021, Pages 29988 - 29994, https://doi.org/10.1016/j.ceramint.2021.07.173.

Conference Abstract

1. 14th ECerS Conference for Young Scientists in Ceramics

"A Sustainable Route for Production of Acid Resistant Fluorine Mica-Based Glass-Ceramic Coatings"

October 20-23, 2021 Novi Sad, Serbia, ISBN 978-86-6253-136-0.